EVALUATING THE STANDARD MODEL OF COSMOLOGY IN LIGHT OF LARGE-SCALE ANOMALIES IN THE COSMIC MICROWAVE BACKGROUND

by

Bingjie Wang

Submitted to the University Honors College

in partial fulfillment of the requirements for the degree of

Bachelor of Philosophy

University of Pittsburgh

2016

UNIVERSITY OF PITTSBURGH

UNIVERSITY HONORS COLLEGE

This thesis was presented

by

Bingjie Wang

It was defended on

April 15, 2016

and approved by

Arthur Kosowsky, Professor, Department of Physics and Astronomy

Carlos Badenes, Assistant Professor, Department of Physics and Astronomy

Jeffrey A Newman, Associate Professor, Department of Physics and Astronomy

Craig Copi, Instructor, Department of Physics, Case Western Reserve University

Thesis Advisor: Arthur Kosowsky, Professor, Department of Physics and Astronomy

EVALUATING THE STANDARD MODEL OF COSMOLOGY IN LIGHT OF LARGE-SCALE ANOMALIES IN THE COSMIC MICROWAVE BACKGROUND

Bingjie Wang, BPhil

University of Pittsburgh, 2016

The establishment of the standard model of cosmology represents great observational and theoretical achievements; at the same time, possible deviations from the standard model are sought. In this thesis, two anomalies are studied:

The late-time integrated Sachs-Wolfe effect—a few percent of the total temperature fluctuations generated by evolving gravitational potentials—is a signature of dark energy in a spatially flat universe. Its strongest detection comes from the average microwave background temperature in the sky directions of superclusters and supervoids seen in the Sloan Digital Sky Survey, which is claimed to be larger than expected. We compute the maximum expected average temperature signal by treating the signal due to large-scale structures as a Gaussian random field, and including correlations between different physical contributions to the temperature fluctuations and between different redshift ranges of the evolving gravitational potentials. Our model confirms that the observed average temperatures are unexpectedly large, but reduces the statistical significance of this discrepancy. Comparing with other measurements, none of which has yielded a detection with the same large discrepancy, our work suggests that a large signal is less unusual to occur than previously thought.

The latter anomaly refers to a 7% asymmetry of fluctuation power between two halves of the sky found in full-sky maps of the microwave background temperature field. A common phenomenological model for this asymmetry is an overall dipole modulation of statistically isotropic fluctuations, which produces particular off-diagonal correlations between multipole

coefficients. We compute these correlations and construct estimators for the amplitude and direction of the dipole modulation. Applying these estimators to various cut-sky temperature maps from Planck and WMAP data shows consistency with a dipole modulation, differing from a null signal at 2.5σ, with an amplitude and direction consistent with previous fits based on the temperature fluctuation power. The signal is scale dependent, with a statistically significant amplitude at angular scales larger than 2 degrees. Future measurements of microwave background polarization and gravitational lensing can increase the significance of the signal. If the signal is not a statistical fluke in an isotropic Universe, it requires new physics beyond the standard model of cosmology.

TABLE OF CONTENTS

LIST OF TABLES

LIST OF FIGURES

1.0 INTRODUCTION

1.1 A STANDARD MODEL OF COSMOLOGY

Cosmology is the study of the universe as a whole: its origin, evolution, and ultimate fate. A wealth of information coming from the theoretical and experimental achievements has transformed cosmology into a fertile data-driven field over the past decades. At the center of this revolution lies the observation of the cosmic microwave background (CMB)—the afterglow of the Big Bang present today as a 2.7K thermal background, which so far provides the cleanest picture of the very early universe.

CMB is widely regarded as one of the strong evidence for the Big Bang cosmological model because its spectrum, first being accurately measured by the The COsmic Background Explorer (COBE) satellite [61], has the shape a black body spectrum. This means that the temperature of the universe must have been very high in the past, which matches with the description provided by the Big Bang model: The universe at the beginning is a hot soup of plasma—the temperature was so high that electrons could not bind to protons to form neutral hydrogen atoms, and photons interact with electrons through Thomson scattering:

$$\gamma + e^- \rightarrow \gamma + e^- \tag{1.1}$$

As the universe expands, it gradually cools down. At the the epoch of recombination, the time at which the baryonic component of the universe goes from being ionized to being neutral, a sudden drop in free electron density occurs. Photons decouple from electrons when the mean free path of the photons, defined in terms of n_e, the number density of free electrons, and δ_e, the Thomson cross-section,

$$\lambda = \frac{1}{n_e \delta_e} \tag{1.2}$$

was approximately equal to the horizon size of the universe H^{-1}.

At this stage, photons are able to steam freely, producing the CMB as we see today. Surrounding every observer in the universe is a last scattering surface (LSS). As CMB photons travel from the LSS to the observer, they have the chance to interact with various effects—those which happen on the LSS are considered as primordial effects, whereas those which happen between the LSS and the observer are considered as late-time effects. Further discussion is presented in Chap. 2.

A parametrization of the Big Bang model is the ΛCDM model. It is often referred to as the standard model of Big Bang cosmology. The model has six free parameters: $\Omega_b h^2$ and

Parameters	Definitions
$\Omega_b h^2$	baryon density
$\Omega_c h^2$	dark matter density
τ	reionization optical depth
$\mathrm{In}(10^{10} A_s)$	primordial curvature perturbations
n_s	scalar spectral index
H_0	Hubble constant

Table 1.1: The six free parameters in the ΛCDM model.

$\Omega_c h^2$, as their names indicate, quantify the matter composition of the universe, τ refers to the time at which the first stars formed, $\mathrm{In}(10^{10} A_s)$ and n_s quantify the amplitude and slope of primordial density fluctuations, and H_0 describes the expansion of the universe.

Great efforts have been dedicated to the determinations of the values of these parameters. WMAP [9], Planck [70], combined with ground-based telescopes such as ACT [51] and SPT [16], provides precise measurement of the CMB that allows us to constrain the parameters with an unprecedented accuracy. Much of these studies are carried out through the CMB temperature power spectrum.

1.2 CMB POWER SPECTRUM

The fluctuations in the CMB are assumed to arise from some random statistical process, and therefore the exact pattern of fluctuations we see from our point in the universe is not of our interest. Rather, a theory of cosmology predicts an underlying distribution, of which our visible sky is a single statistical realization. For this purpose, it is conventional to expand the temperature fluctuations of a CMB map $\delta T/T(\theta, \phi)$ in spherical harmonics:

$$\frac{\delta T}{T} = \sum_{\ell=0}^{\infty} \sum_{m=-\ell}^{\ell} a_{\ell m} Y_{\ell m}(\theta, \phi) \tag{1.3}$$

where $a_{\ell m}$ are the temperature multipole coefficients, and $Y_{\ell m}(\theta, \phi)$ are the spherical harmonics of degree ℓ and order m, arising from solving the angular portion of Laplace's equation. The order m describes the angular orientation of a fluctuation mode, while the degree (or multipole) ℓ describes its characteristic angular size, which generally can be linked to angular scale through the relation $\theta \approx 180^\circ/\ell$.

Using Eq. (1.3), we can write down perhaps the most important statistical property of the fluctuations, the two-point correlation function $C(\theta)$. Consider two points on the LSS: Relative to an observer, they are in the directions $\hat{n}$ and $\hat{n}'$, and are separated by an angle θ given by the relation $\cos\theta = \hat{n} \cdot \hat{n}'$. $C(\theta)$ is defined as the multiplication of the values of $\delta T/T$ at the two points, averaging over all points separated by the angle θ:

$$C(\theta) = \left\langle \frac{\delta T}{T}(\hat{n}) \frac{\delta T}{T}(\hat{n}') \right\rangle_{\hat{n}\cdot\hat{n}'=\cos\theta} \tag{1.4}$$

$$C(\theta) = \frac{1}{4\pi} \sum_{l=0}^{\infty} (2\ell + 1) C_\ell P_\ell(\cos\theta) \tag{1.5}$$

where P_ℓ are the usual Legendre polynomials.

The expansion coefficients in Eq. (1.3),

$$a_{\ell m}^T = \frac{1}{T_0} \int d(\hat{n}) T(\hat{n}) Y_{\ell m}^*(\hat{n}) \tag{1.6}$$

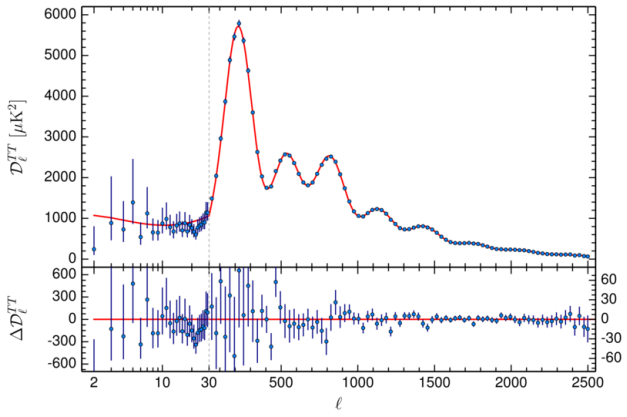

Figure 1.1: Temperature power spectrum from Planck [78].

are averaged over m to obtain the best estimate of temperature power spectrum:

$$C_\ell^{TT} = \frac{1}{2\ell+1} \sum_{m=-\ell}^{\ell} (a_{\ell m}^{T*} a_{\ell m}^{T}) \tag{1.7}$$

This gives the best estimate since the power spectrum in a universe with no preferred direction is expected to be independent of m. The fact that there exist only $(2\ell+1)$ modes with which to detect the power at multipole ℓ sets a fundamental limit in determining the power. This is known as the cosmic variance:

$$\frac{\Delta C_\ell}{C_\ell} = \sqrt{\frac{2}{2\ell+1}} \tag{1.8}$$

However, to consider the full uncertainty we must include additional factors as instrumental noise, finite beam resolution, and for partial sky surveys, the fact that only a finite fraction of the full sky is observed.

By convention, the quantity that is usually plotted, as shown in Fig. 1.1, is

$$\Delta T^2 \equiv \frac{\ell(\ell+1)}{2\pi} C_\ell T_{CMB}^2 \tag{1.9}$$

where T_{CMB} is the blackbody temperature of the CMB. This is often referred to as the TT (temperature-temperature correlation) spectrum.

1.3 THE INTEGRATED SACHS-WOLFE EFFECT

As CMB photons from LSS travel across the universe, they may be gravitationally redshifted, which result in the integrated Sachs-Wolfe effect (ISW) [82]. It is often separated into two contributions, namely the early-time ISW and the late-time ISW. The physics is the same. Those terms are labeled such in order to distinguish between primodial and late-time effects—early ISW occurs when there is still enough radiation around, while the late ISW occurs due to the time-evolving gravitational potentials driven by dark energy, as there is a net change in energy to photons traversing an underdense or overdense region. The late ISW is described by the following integral along line-of-sight:

$$\Theta(\hat{\mathbf{n}}) \equiv \frac{\Delta T}{T_0} = -2 \int_0^{\chi^\star} d\chi g(\tau) \dot{\Phi}(\chi \hat{\mathbf{n}}, \eta_0 - \chi) \tag{1.10}$$

where $g(\tau) = e^{-\tau(\eta_0 - \chi)}$ is the visibility function as a function of the optical depth τ, the derivative of the Newtonian gravitational potential Φ is with respect to the conformal time, η_0 is the present value of the conformal time, $\chi^\star$ is the comoving distance to the surface of last scattering, and T_0 is the isotropic CMB blackbody temperature, corresponding to the multipole moment $\ell = 0$. The ISW effect is mostly responsible for temperature fluctuations on large angular scales ($\theta > 3^\circ$).

Additionally, once non-linear structures such as galaxy clusters form, linear perturbation theory breaks down. The contribution to the ISW from non-linear perturbations is called the Rees-Sciama effect.

In a spatially flat universe, the late ISW effect can be used as an independent probe for dark energy since for cosmological models where $\Omega_m = 1$, gravitational potentials remain constant during linear structure formation, and the late ISW signal is negligible to first order.

The most direct way for detecting the ISW effect is the determination of the cross-correlation or the cross-angular power spectrum between the CMB temperature and the density of tracer objects such as galaxies. Such approach has been applied to WMAP as well as Planck data. In the Planck 2015 result [76], they include additional galaxy and AGN catalogues, correlated with the four Planck CMB maps, and yields a detection of the ISW signal at 2.9σ. In addition, they improve the characterization of the ISW effect through the

ISW-lensing bispectrum. The higher signal-to-noise ratio of the Planck 2015 temperature data and the new polarization data help to reconstruct the Planck lensing signal. With such help, the detection reaches approximately 3σ. When combining the Planck ISW-lensing with the cross-correlation of the Planck CMB with LSS tracers, a total detection of the ISW effect at 4σ is obtained. Those detections of the ISW effect are all at the expected level for the ΛCDM model.

An alternative approach consists of stacking CMB fields centered on known superclusters or supervoids [35]. This gives (arguably) the clearest ISW detection to date. However, it has been argued that this detected signal is 3.3σ away from a theoretical ΛCDM estimate obtained by performing large N-body simulations [31]. Chap. 2 presents our investigation of this discrepancy based on Gaussian approximation [3].

1.4 THE HEMISPHERICAL POWER ASYMMETRY

ΛCDM gives us a flat, isotropic and homogeneous universe seeded by Gaussian and adiabatic fluctuations. However, examination of the WMAP data reveals that there exhibits more large-scale power on one half of the CMB temperature sky than the other [28], which is also sequentially confirmed in Planck data [75]. This possible violation to the standard cosmological scenario has profound implications for our understanding of the physical nature of the universe and the initial conditions of structure formation.

The power asymmetry has been detected using multiple techniques, including spatial variation of the temperature power spectrum for multipoles up to $\ell = 600$ [75] and measurements of the local variance of the CMB temperature map [6, 2]. For $\ell > 600$, the amplitude of the power asymmetry drops quickly with ℓ [30, 2].

A phenomenological model for the hemispherical power asymmetry is a statistically isotropic sky $\Theta(\hat{\mathbf{n}})$ times a dipole modulation of the temperature anisotropy amplitude:

$$\tilde{\Theta}(\hat{\mathbf{n}}) = (1 + \hat{\mathbf{n}} \cdot \mathbf{A})\, \Theta(\hat{\mathbf{n}}), \tag{1.11}$$

where the vector $\mathbf{A}$ gives the dipole amplitude and sky direction of the asymmetry [33].

Both WMAP [27, 42] and Planck [75] show a dipole modulation with the amplitude $|\mathbf{A}| \simeq 0.07$ along the direction $(l, b) \simeq (220^\circ, -20^\circ)$ in galactic coordinates, with a significance at a level $\geq 3\sigma$. Further analysis at intermediate scales $100 < \ell < 600$ shows that the amplitude of the dipole modulation is also scale dependent [38].

Chap. 3 presents our work on utilizing off-diagonal correlations between multipole components to construct estimators for the Cartesian components of the vector $\mathbf{A}$, and applying the estimators to foreground-cleaned Planck CMB temperature maps [4].

2.0 GAUSSIAN APPROXIMATION OF PEAK VALUES IN THE INTEGRATED SACHS-WOLFE EFFECT

This chapter is reproduced in part with permission from S. Aiola, A. Kosowsky, and B. Wang. Gaussian approximation of peak values in the integrated Sachs-Wolfe effect. Phys. Rev. D, 91(4):043510, February 2015.

2.1 BACKGROUND

In 2008, [35] (GNS08, hereafter) employed a photometric analysis of stacked CMB patches from the WMAP 5-year sky maps [41] centered on 100 superstructures (50 biggest superclusters and 50 biggest supervoids) detected in the Sloan Digital Sky Survey (SDSS) Data Release 6 [1]. This SDSS Data Release covers a sky area of 7500 square degrees in a redshift range $0.4 < z < 0.75$. GNS08 reported a mean temperature fluctuations of $\overline{T} = 9.6$ μK, showing a departure from the null signal at a significance of 4.4σ.

However, analytical estimates of the stacked late-ISW signal in a comoving volume that corresponds to that probed by GNS08 gives an average signal of $\overline{T} = 2.27 \pm 0.14 \mu K($ [31], FHN13 hereafter). The error here is due to cosmic variance. This results a greater than 3σ discrepancy as compared to the GNS08 measurement. Since then other cosmological models have been proposed to resolve this discrepancy, such as primordial non-Gaussianities [39] and $f(R)$ gravity theories [13], though neither seems to offer an adequate explanation for the strong ISW signal detected.

A less interesting but more plausible possibility is that the strong detected signal is the

result of correlations of the late ISW signal with other sources of temperature anisotropy, which may boost the mean temperature of the identified top-ranked peaks. The current theoretical predictions of the stacked late-ISW signal of FHN13 do not include correlations between ISW temperature fluctuations formed at different redshifts. However, we expect a non-negligible correlation between the late-ISW signal, traced by superstructures in GNS08 in the redshift range $0.4 < z < 0.75$, and the late-ISW effect due to structures at either higher or lower redshift. In addition, high-redshift fluctuations are also partially correlated with the secondary temperature anisotropies, at a level that depends on the underlying cosmological model.

In this chapter, we provide a complete description of these correlations through simulated skies based on linear perturbation theory. Temperature fluctuations on large scales result from gravitational potential perturbations in the linear regime (see [20] for alternative proposal). If the primordial perturbations are a Gaussian random field, which appears to be an excellent approximation to the observed large-scale structure [69], the statistical properties of the CMB sky on large angular scales are completely specified by the temperature power spectrum C_ℓ^{TT}. We generate Gaussian random realizations of the CMB sky using the linear power spectra for its various physical components, including correlations between them. This is an easy computational process, in contrast to extracting large-angle late-ISW maps from large-box N-body cosmological simulations [86, 43]. This approach allows full characterization of cosmic variance with a random sample of simulated skies, and it automatically accounts for the effects of the largest-scale perturbation modes beyond the reach of N-body simulations.

Our simulated late-ISW mean peak temperature signal is consistent with previous estimates, but with a wider spread of values. Correlations between temperature signals increase the expected mean value as well as the spread slightly. The main reason for this larger spread, however, is the noise associated to the uncorrelated fluctuations at scales of our interest, and thus reduces the statistical significance of the discrepancy between theory and experiment to around 2.5σ when compared with our measured values from CMB maps.

My involvement in this work is within the scope of Sec. 2.2 and Sec.2.3—developing an algorithm to generate realistic temperature maps, including spatial filtering and all correla-

tions between temperature components, and applying the pipeline to simulate distributions of late-ISW mean peak temperatures. For the completeness of this presentation, applying the same procedure to the Planck CMB temperature maps is stated in Appendix . This step guarantees that the discrepancy between theoretical estimates and the measured signal is not due to different analysis procedures. Sec. 2.5 concludes with a discussion of possible sources of systematic errors, a comparison with other late-ISW detection techniques.

2.2 CORRELATED COMPONENTS OF THE TEMPERATURE SKY

In the ΛCDM paradigm, different physical processes contribute to temperature fluctuations over a wide range of angular scales; the CMB temperature sky is well approximated by the sum of correlated Gaussian random fields, one for each physical component, such that

$$\begin{aligned} \langle a^i_{\ell m}, a^{i\star}_{\ell' m'} \rangle &= \delta_{\ell\ell'}\delta_{mm'}C^{ii}_\ell \\ \langle a^i_{\ell m}, a^{j\star}_{\ell' m'} \rangle &= \delta_{\ell\ell'}\delta_{mm'}C^{ij}_\ell \end{aligned} \tag{2.1}$$

where i and j are the components making up the observed temperature field $\Theta(\hat{\mathbf{n}}) = \sum_i \sum_{\ell m} a^i_{\ell m} Y_{\ell m}$ and the power spectra satisfy the condition $C^{ii}_\ell C^{jj}_\ell \geq (C^{ij}_\ell)^2$ [45]. This set of power spectra specify the covariance matrix of the temperature given a cosmological model. For the purposes of this work, we consider a 2-component sky described by a symmetric 2 by 2 covariance matrix. The first component, $C^{1,1}_\ell$, is always the late-ISW component of the temperature field, corresponding to the GNS08 redshift range (ISW–in, hereafter). As for the second component, $C^{2,2}_\ell$, we consider two distinct cases:

(i) *Case A*: only late-ISW generated outside the probed redshift range, corresponding to $0 < z < 0.4$ and $0.75 < z < 10$ (ISW–out, hereafter);

(ii) *Case B*: primary and secondary anisotropies generated outside the probed redshift range. Specifically, we consider the sum of ISW–out, early ISW after recombination, and Sachs-Wolfe, intrinsic and Doppler contributions at last scattering.

The off-diagonal terms $C^{1,2}_\ell$ are calculated according to the specific case we consider. For a spatially flat, ΛCDM cosmological model with the best-fit Planck+WP+HighL parameters [74] we compute the covariance matrix in Eq. (2.1) with the numerical Boltzmann code

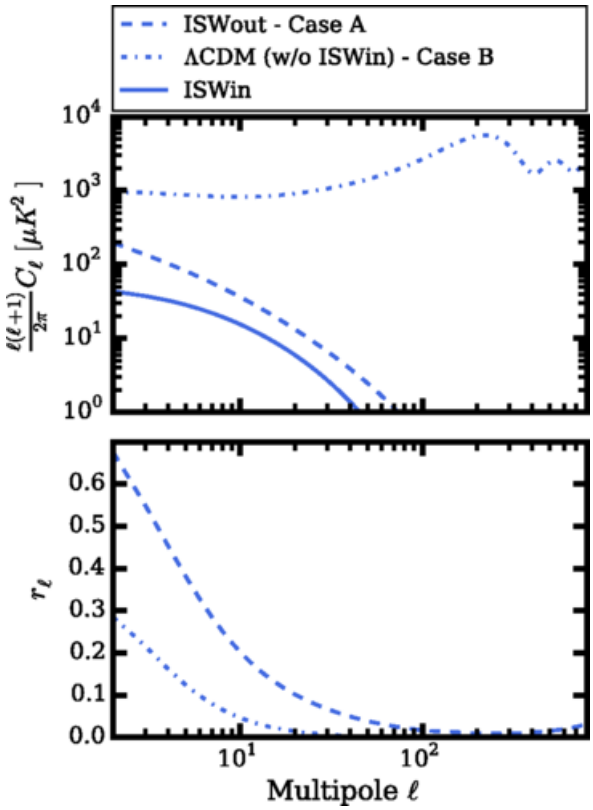

Figure 2.1: Top: Angular power spectra in ΛCDM, for the ISW effect due to structure in the redshift range $0.4 < z < 0.75$ ("ISW–in"), ISW effect outside of this redshift range ("ISW–out"), and all temperature perturbation components except for ISW–in (yellow). Bottom: Correlation coefficients between ISW–in and ISW–out, and between ISW–in and all other temperature perturbation components.

`CLASS v2.2`[1] [10] (including the nonlinear effects calculated with `Halofit` [83], although we have verified that these do not affect our results.) The correlated harmonic coefficients are generated via Cholesky decomposition as

$$\begin{aligned} a^i_{\ell m} &= \sum_{k=1}^{2} A_{\ell,ik}\zeta_k \\ a^T_{\ell m} &= a^1_{\ell m} + a^2_{\ell m} \end{aligned} \tag{2.2}$$

[1] `http://class-code.net/`

where ζ_k is a column vector composed of 2 complex gaussian random numbers with zero mean and unit variance, and A_ℓ is a lower-diagonal real matrix which satisfies $C_\ell = A_\ell^T A_\ell$. The $a^1_{\ell m}$ are the harmonic coefficients corresponding to the ISW–in component alone.

In Fig. 2.1, we plot the unfiltered covariance matrix components as function of the multipole ℓ. The top panel shows the diagonal terms. Note that the signal of interest, ISW–in, has a lower amplitude compared than the other components at all multipoles. Thus, the statistics of temperature peaks for an unfiltered map are completely dominated by the anisotropies generated at last scattering. A wise choice for an ℓ-space filter is required (see below, Sec. 2.3). The bottom panel shows the off-diagonal terms; we plot the normalized correlation coefficient

$$r_\ell \equiv \frac{C_\ell^{ij}}{\sqrt{C_\ell^{ii} C_\ell^{jj}}} \tag{2.3}$$

which satisfies the condition $|r_\ell| \leq 1$. The correlation matrix cannot be considered diagonal, especially at low ℓ values. In principle we expect a negative cross-correlation on large scales (i.e. $r_\ell < 0$) due to the Sachs-Wolfe component: If we consider the entire late-ISW contribution (i.e., $0 < z < 10$), the cross-spectrum is dominated by the ISW-SW term, which gives an overall anti-correlation. In the case of interest (where we consider shells of late-ISW signal), the dominant part is the correlation between ISW–in and ISW–out. Notice that $r_\ell^{\rm CaseA}/r_\ell^{\rm CaseB} \simeq \sqrt{C_\ell^{2,2({\rm CaseB})}/C_\ell^{2,2({\rm CaseA})}}$, which implies that the mean value of the stacked signal is mainly enhanced by the ISW–out component. This peculiar effect is attributed to the wide range of $k-$modes, which couples the fluctuations of neighboring redshift regions. On the other hand, the mildly correlated primary fluctuations dominate the statistical error in averaged peak values.

2.3 METHODOLOGY AND ANALYSIS

The multipole region of our interest is dominated by cosmic variance. This problem is difficult to characterize using N-body simulations, so we generate random temperature maps from the power spectra and correlations to construct the statistical distribution of ISW mean

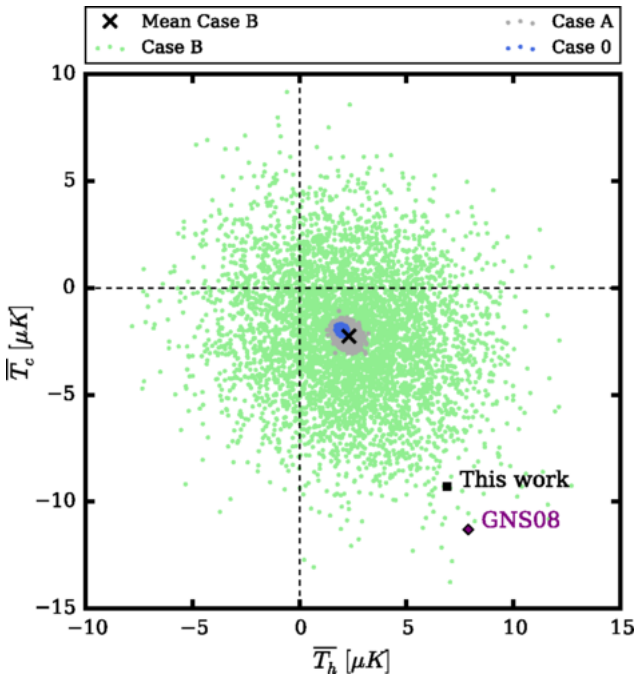

Figure 2.2: The mean value of the filtered CMB temperature at the locations of the top 50 cold spots $\overline{T_{\rm cold}}$ and top 50 hot spots $\overline{T_{\rm hot}}$ of the ISW–in map component, corresponding to the late-ISW signal from structures in the redshift range $0.4 < z < 0.75$, for a sky fraction $f_{sky} = 0.2$. Plotted are $(\overline{T_{\rm hot}}, \overline{T_{\rm cold}})$ for 5000 randomly generated skies with all contributions to the CMB signal (green points). The red cross is at the location of the mean values of $\overline{T_{\rm cold}}$ and $\overline{T_{\rm hot}}$ for the 5000 model skies. For comparison, we plot 5000 model skies generated using only the ISW–in signal (grey points), and 5000 skies generated using the full late late-ISW signal but no other temperature components (blue points). Also displayed are the measured values from GNS08 (purple diamond) and from the analysis in Sec. 2.3 using Planck data (black square).

peak amplitudes. The procedure described in this section is based on the FHN13 analysis, adapted to multi-component correlated sky maps.

2.3.1 Harmonic-Space Filtering

In the GNS08 redshift range ($0.4 < z < 0.75$), the expected cross-correlation spectrum peaks at $\ell \simeq 20$ ($\theta \simeq 4^\circ$) ([39], HMS13 hereafter), which motivated the use of a compensated top-hat filter of 4° radius to enhance the signal [36].

To isolate the late-ISW peak signal in ℓ-space, we apply the 4° compensated top-hat filter adopted by GNS08:

$$F(\theta) = \begin{cases} (2\pi(1-\cos\theta_F))^{-1}, & 0 < \theta < \theta_F, \\ \\ -(2\pi(\cos\theta_F - \cos\sqrt{2}\theta_F))^{-1}, & \theta_F < \theta < \sqrt{2}\theta_F, \end{cases} \tag{2.4}$$

where $\theta_F = 4^\circ$ is the characteristic filter radius. By performing a Legendre transform of the real-space filter $F(\theta) \to F_\ell = \int F(\theta)\mathcal{P}_\ell(\cos\theta)d\cos\theta$, we can compute a full-sky filtered map simply by rescaling the covariance matrix, $C_\ell \to C_\ell F_\ell^2 B_\ell^2$, which also uses an additional Gaussian beam smoothing B_ℓ with `FWHM`$= 30'$ adopted by PLK13 to match the WMAP resolution. The compensated top-hat filter does not give a sharp cutoff in multipole space. However, it drops off faster than ℓ^{-2}, which ensures the suppression of the small-scale fluctuations. At the scales enhanced by the filter $\ell \simeq 10 - 30$, the portion of the temperature fluctuations uncorrelated with the ISW–in signal for Case B is approximately one order of magnitude larger than that for Case A, with a resulting increase in the scatter of the mean peak statistic.

2.3.2 Simulation Pipeline

To identify the peaks of the late-ISW temperature fluctuations in the CMB sky map, GNS08 used the distribution of luminous red galaxies in `SDSS DR6` and looked for overdense and underdense regions. The top-ranked 100 superstructures identified in the sample have a median radial length calculated at $z = 0.5$ of $R_v \simeq 85Mpc$ and $R_c \simeq 25Mpc$ for voids and clusters respectively. The corresponding normalized fluctuations of the gravitational potential are of the order $\Phi \simeq 10^{-4}$ [36]. These gravitational potential fluctuations are still in the linear regime for standard structure growth.

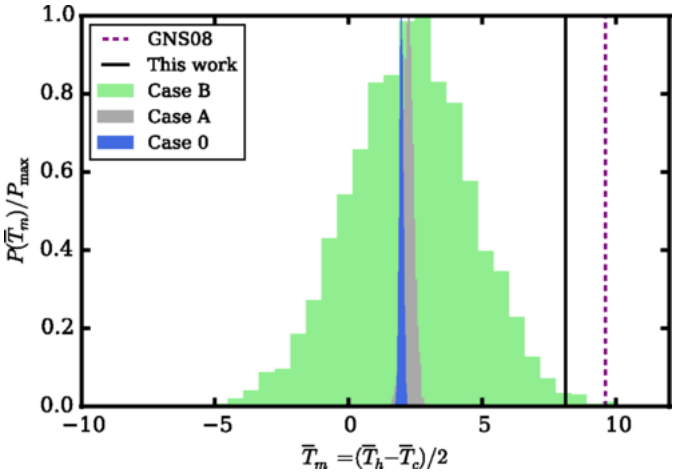

Figure 2.3: The combined mean value of the filtered CMB temperature at the locations of the top 50 cold spots and top 50 hot spots of the ISW–in map component, corresponding to the late-ISW signal from structures in the redshift range $0.4 < z < 0.75$, for a sky fraction $f_{sky} = 0.2$. Plotted are the distributions (normalized to the maximum value) of the combined mean temperature $(\overline{T_{\rm hot}} - \overline{T_{\rm cold}})/2$ obtained from 5000 simulated skies, for the three difference cases considered in this work. Also displayed are the measured values from GNS08 (purple vertical line) and from the analysis in Sec. **??** using Planck data (black vertical line).

Assuming perfect efficiency in detecting and ranking superstructures from large-scale structure distribution data, the observed GNS08 signal should match the theoretical expectation from averaging the CMB temperature fluctuations traced by the 100 biggest fluctuations in the filtered late-ISW map over the redshift range of the survey [31]. We generate correlated pairs of filtered random Gaussian maps, one for the ISW–in component and one for the other linear components of the temperature sky, using multipoles in both power spectrum $\ell \leq 800$; we use `HEALPix`[2] [34] with `NSIDE`=256. From the filtered ISW–in map, we identify the 50 hottest maxima and 50 coldest minima in a sky region of area $f_{\rm sky} = 0.2$, corresponding to the sky fraction of the `SDSS DR6` survey. Maxima and minima are identified pixel-by-pixel, testing whether or not the temperature of the central pixels is the greatest

[2] `http://healpix.sf.net`

or the smallest of the 8 surrounding pixels. Finally, we take the pixels corresponding to these extrema and average their values in the full sky map consisting of the sum of the two correlated random maps. We find the average of the 50 hottest ISW–in maxima $\overline{T_h}$ and 50 coldest ISW–in minima $\overline{T_c}$ separately, and we also compute the combined mean value as $\overline{T_m} = (\overline{T_h} - \overline{T_c})/2$. For comparison, we also calculate the same quantities for the ISW–in map only, which we call Case 0. This procedure is performed on an ensemble of 5000 random generated skies.

The procedure adopted here gives an upper bound on the theoretical signal from clusters and voids identified in any specific tracer of large-scale structure: we simply assume that the 50 largest voids and 50 largest clusters in a sky region are correctly identified. Any error in identifying these features will lead to a smaller mean signal.

2.4 RESULTS AND COMPARISON WITH PREVIOUS WORKS

The results of our simulations are presented in Table 2.4 and visually summarized in Figs 2.2 and 2.3. As expected for random realizations of a Gaussian field, $|\overline{T_h}| = |\overline{T_c}|$. The mean peak signal for the full simulated sky maps (Case B) is 2.30 ± 2.32 μK, compared to the GNS08 measurement of 9.6 μK, a discrepancy at a significance of 3.1σ. Our discrepancy is about the same size as previous analyses, but the significance is somewhat lower. This is due to our inclusion of all components in the microwave temperature map and their correlations, which increases the uncertainty in our predicted values. The central value of our ISW–in peak signal, 1.97 μK (Case 0), is lower by 0.30 μK than the signal predicted in FHN13, which is expected due to a difference in the underlying cosmological models used. However, the difference is small compared to the statistical uncertainty for the full sky signal (Case B). The central value of our full-sky peak signal is also higher than the ISW–in peak signal by 0.33 μK; this difference is due to the correlations between the ISW–in signal and the other components which are included in the Case B peak signal.

The original late-ISW peak analysis in GNS08 used WMAP sky maps, and PLK13 confirmed the measured value using Planck data. Here we obtain the measured late-ISW

Case	$\overline{T_h}$ $[\mu K]$	$\overline{T_c}$ $[\mu K]$	$\overline{T_m}$ $[\mu K]$
Case 0	1.97 ± 0.09	-1.97 ± 0.09	1.97 ± 0.07
Case A	2.23 ± 0.25	-2.23 ± 0.25	2.23 ± 0.20
Case B	2.30 ± 3.1	-2.30 ± 3.1	2.30 ± 2.32
FHN13	-	-	2.27 ± 0.14
GNS08	7.9 ± 3.1	-11.3 ± 3.1	9.6 ± 2.22

Table 2.1: Results from Gaussian random skies, stacked on peaks of the ISW–in signal (the ISW generated for structure in the redshift range $0.4 < z < 0.75$). The simulated skies are constructed from the angular power spectra in the standard ΛCDM cosmology, smoothed with a Gaussian beam of FWHM 30' and a compensated top hat filter of radius 4°, Eq. (2.4). We report the mean and the standard deviation of the stacks on the locations of the 50 hottest ISW–in spots $\overline{T_h}$, 50 coldest ISW–in spots $\overline{T_c}$, and the mean magnitude for all 100 spots $\overline{T_m}$, calculated from 5000 random realizations of the microwave sky, including correlations between the ISW–in signal and other sky components. These values are presented for ISW–in skies only (Case 0), ISW–in plus ISW–out skies (Case A), and realistic skies including early ISW, intrinsic, and Doppler contributions to the sky temperature (Case B). The theoretical prediction from FHN13 and the measured value from GNS08 are reported for comparison.

signal from publicly available foreground-cleaned maps based on Planck and Planck+WMAP data, using the same sky locations as GNS08. The purpose of this re-analysis is testing the significance of the discrepancy by using the same analysis pipeline as the simulations in Sec. 2.3, to ensure that the difference between the model and the measured value is not due to any inconsistency in how the data and simulations are treated.

We use four different foreground-cleaned CMB temperature maps, based on different component separation approaches. Two are public CMB temperature maps from the `Planck` collaboration[3], namely `SMICA` and `NILC` [73]. The other two maps are based on the `LGMCA`

[3] http://www.sciops.esa.int/wikiSI/planckpla

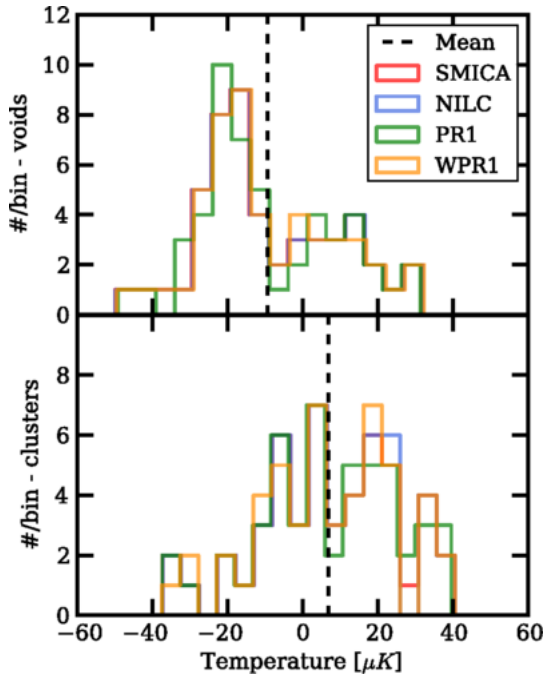

Figure 2.4: Histograms of pixel temperatures centered on superstructures identified by GNS08, measured using 4 different foreground-cleaned filtered CMB maps. Top panel: measured temperatures at locations of voids in the GNS08 catalog; the dashed vertical line indicates the mean temperature. Bottom panel: the same for locations of clusters.

method[4] from the recent work in Ref. [11]. The `PR1` map uses only `Planck DR1` data [72], and the `WPR1` map uses both `Planck DR1` and `WMAP9` dat [40].

We process these four maps in the same fashion:

(i) we apply a gaussian beam smoothing in harmonic space to the map defined as $B_\ell = B_\ell(30')/B_\ell(\text{map})$ where $B_\ell(\text{map})$ is the effective beam of the released map; this allows us to take into account for the finite resolution of the instrument, and hence matching the overall smoothing applied to the simulated maps. We also filter out the small-scale fluctuations by setting the harmonic coefficients of the map $a_{\ell m} = 0$ for $\ell > 800$;

(ii) the preprocessed map is then masked using the released `Planck` mask `U73`, avoiding contaminates from bright point sources;

[4] http://www.cosmostat.org/CosmoStat.html

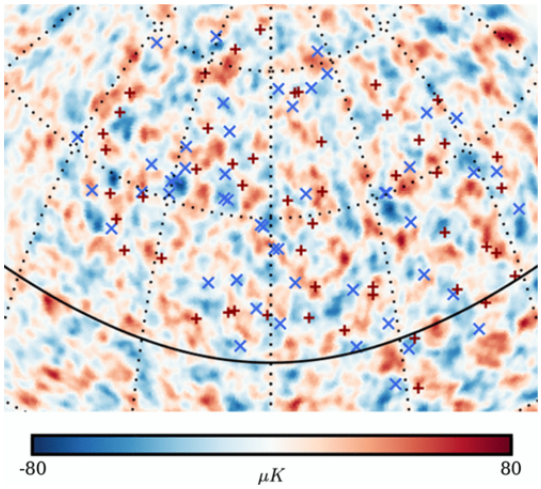

Figure 2.5: The filtered SMICA-Planck CMB temperature map, in a Mollweide projection in ecliptic coordinates. The galactic region and point sources have been masked with the U73-Planck mask. The resolution of the HEALPix maps is NSIDE= 256. The locations of superclusters (red "+") and supervoids (blue "x") from the GNS08 catalog are also shown.

(iii) the masked map is filtered in harmonic space using the compensated top-hat filter F_ℓ and repixelized to `NSIDE`=256;

(iv) we read the temperature values of the pixels corresponding to the cluster/void positions used in GNS08 [5].

Fig. 2.5 shows the filtered `SIMCA` map in a Mollweide projection in ecliptic coordinates; superstructure locations from GNS08 are marked. In Fig. 2.4, we plot the histogram of the temperature values for voids and clusters separately for the four analyzed maps. The measured values are used to calculate the quantities $\overline{T_c}$, $\overline{T_h}$ and $\overline{T_m}$ given in Table II. Different component separation methods quantify the effects of residual foreground contamination. We measure the fluctuations of the average temperature signal for different maps and use the variance of these fluctuations $\sigma_{\rm FG}$ as an estimate of the error due to foregrounds. The temperature values are extremely stable and fluctuations are always within 1% (see also Fig. 4), suggesting that the temperature variations are predominantly cosmological. Our

[5] http://ifa.hawaii.edu/cosmowave/supervoids/publications-and-data/

Map	$\overline{T_h}$ $[\mu K]$	$\overline{T_c}$ $[\mu K]$	$\overline{T_m}$ $[\mu K]$
NILC	6.9	-9.4	8.1
SMICA	7.0	-9.4	8.2
PR1	6.9	-9.3	8.1
WPR1	6.9	-9.2	8.0
MEAN	6.89	-9.33	8.11
σ_{FG}	0.01	0.09	0.04

Table 2.2: Mean temperature deviations for GNS08 cluster and void locations, for four temperature maps with different foreground cleaning procedures.We estimate the mean and standard deviation σ_{FG} from the four different maps.

mean peak temperature values are smaller than those reported by GNS08 and PLK13 by around 1.5 μK, which is within the 1σ uncertainty. Such a difference is driven mainly by details of the filtering procedure.

The results of our simulations and our measured signals, shown in Fig. 2.2 and Fig. 2.3, can be summarized as

(i) The departure of the measurements from a null signal has decreased somewhat compared to previous analyses. It corresponds to a detection significance of 2.2σ, 3.0σ and 3.5σ for clusters, voids and combined, respectively;

(ii) The measurements are higher than the expected maximum signal in ΛCDM cosmology at a level of 1.5σ, 2.3σ and 2.5σ for clusters, voids and combined, respectively;

(iii) The asymmetry between the measured signal for voids and clusters is not statistically significant, being smaller than 1σ.

For these estimates, we consider foregrounds contamination and cosmic variance from simulations to be uncorrelated; hence we take $\sigma_{\rm tot} = \sqrt{\sigma^2_{\rm FG} + \sigma^2_{\rm sim}}$, but the residual foreground error is small compared to the cosmic variance uncertainty.

2.5 DISCUSSION

Our analysis confirms both the size of the stacked late-ISW signal seen by GNS08 and PLK13, and theoretical predictions for ΛCDM models by FHN13 and HMS13. By using several maps with different foreground subtraction methods, we demonstrate that foreground residuals contribute negligible uncertainty to the measured signal. The theoretical modeling, using correlated Gaussian random fields, is far simpler than previous analyses using N-body simulations, showing that the predicted signal has no significant systematic error arising from insufficient box size or other subtleties of the simulations. Our calculations also include the correlations between the late-ISW signal and other sources of microwave temperature anisotropies, which mildly increases the theoretical mean signal while also increasing the statistical uncertainty. We find a stacked late-ISW signal which is different from null at 3.5σ significance, and a discrepancy between the predicted and observed signal of 2.5σ in Planck sky maps at the peak and void locations determined by GNS08 from SDSS data in the redshift range $0.4 < z < 0.75$.

After this work was published, another stacking analysis using a new catalogue from the CMASS survey is released [53], but such anomaly was not observed. More specifically, the GNS08 supervoid positions, which are selected via photometry, do not coincide with regions abundant in DR10 voids which identified in spectroscopic samples, and no significant imprint was detected when performing the stacking analysis using DR10 CMASS and LOW-Z voids. In short, their results showed that ISW detections with the stacking protocol strongly depend on the properties of the tracer population and the void finder. However, the analysis from Planck DR2 [76], in which the Planck polarization data is used to explore further the origin of the stacking signal, indicates a secondary nature of the stacking signal. At current stage, therefore, it remains an open question in need of future surveys.

3.0 MICROWAVE BACKGROUND CORRELATIONS FROM DIPOLE ANISOTROPY MODULATION

This chapter is reproduced with permission from S. Aiola, B. Wang, A. Kosowsky, T. Kahniashvili, and H. Firouzjahi. Microwave background correlations from dipole anisotropy modulation. Phys. Rev. D, 92(6):063008, September 2015.

3.1 BACKGROUND

A phenomenological model for the hemispherical power asymmetry is a statistically isotropic sky $\Theta(\hat{\mathbf{n}})$ times a dipole modulation of the temperature anisotropy amplitude:

$$\tilde{\Theta}(\hat{\mathbf{n}}) = (1 + \hat{\mathbf{n}} \cdot \mathbf{A})\, \Theta(\hat{\mathbf{n}}), \tag{3.1}$$

where the vector $\mathbf{A}$ gives the dipole amplitude and sky direction of the asymmetry [33]. This phenomenological model has been tested on large scales ($\ell < 100$) with both WMAP [27, 42] and Planck ([75], hereafter PLK13) data, showing a dipole modulation with the amplitude $|\mathbf{A}| \simeq 0.07$ along the direction $(l, b) \simeq (220°, -20°)$ in galactic coordinates, with a significance at a level $\geq 3\sigma$. Further analysis at intermediate scales $100 < \ell < 600$ shows that the amplitude of the dipole modulation is also scale dependent [38].

If a dipole modulation in the form of Eq. (3.1) is present, it induces off-diagonal correlations between multipole components with differing l values. Similar techniques have been employed to study both the dipole modulation [79, 38, 66, 81] and the local peculiar

velocity [52, 7, 77, 44]. We use these correlations to construct estimators for the Cartesian components of the vector **A** as function of the multipole, the derivation of which for a cosmic-variance limited CMB temperature map is presented in Sec. 3.2.

In particular, I contributed to the testing and application of the estimators for the *Planck* temperature maps (Sec. 3.3). The Planck temperature data that are used to obtain the results is described in Sec. 3.4. For the completeness of this presentation, Sec. 3.5, in which we further analyze our result through geometrical test and a power-law model fit, is also included. We estimate the components of the dipole modulation vector and assess their statistical significance, finding departures from zero at the 2 to 3 σ level. The best-fit dipole modulation signal is an unexpectedly good fit to the data, suggesting that we have neglected additional correlations in modeling the temperature sky. We also perform a Monte Carlo analysis to estimate how the dipole modulation depends on angular scale, confirming previous work showing the power modulation becoming undetectable for angular scales less than 0.4°. Finally, Sec. 3.6 gives a discussion of the significance of the results and possible implications for models of primordial perturbations.

3.2 DIPOLE-MODULATION-INDUCED CORRELATIONS AND ESTIMATORS

Assuming the phenomenological model described by Eq. (3.1), the dipole dependence on direction can be expressed in terms of the $l = 1$ spherical harmonics as

$$\hat{\mathbf{n}} \cdot \mathbf{A} = 2\sqrt{\frac{\pi}{3}}(A_+ Y_{1-1}(\hat{\mathbf{n}}) - A_- Y_{1+1}(\hat{\mathbf{n}}) + A_z Y_{10}(\hat{\mathbf{n}})) \tag{3.2}$$

with the abbreviation $A_\pm \equiv (A_x \pm iA_y)/\sqrt{2}$. Expanding the temperature distributions in the usual spherical harmonics,

$$\Theta(\hat{\mathbf{n}}) = \sum_{lm} a_{lm} Y_{lm}(\hat{\mathbf{n}}), \qquad \tilde{\Theta}(\hat{\mathbf{n}}) = \sum_{lm} \tilde{a}_{lm} Y_{lm}(\hat{\mathbf{n}}), \tag{3.3}$$

with the usual isotropic expectation values

$$\langle a^*_{lm} a_{l'm'} \rangle = C_l \delta_{ll'} \delta_{mm'}. \tag{3.4}$$

The coefficients must satisfy $a^*_{lm} = (-1)^m a_{l-m}$ and $\tilde{a}^*_{lm} = (-1)^m \tilde{a}_{l-m}$ because the temperature field is real. The asymmetric multipoles can be expressed in terms of the symmetric multipoles as

$$\tilde{a}_{lm} = a_{lm} + 2\sqrt{\frac{\pi}{3}} \sum_{l'm'} a_{l'm'} (-1)^m \int d\hat{\mathbf{n}}\, Y_{l-m}(\hat{\mathbf{n}}) Y_{l'm'}(\hat{\mathbf{n}}) [A_+ Y_{1-1}(\hat{\mathbf{n}}) - A_- Y_{1+1}(\hat{\mathbf{n}}) + A_z Y_{10}(\hat{\mathbf{n}})]. \tag{3.5}$$

The integrals can be performed in terms of the Wigner 3j symbols using the usual Gaunt formula,

$$\begin{aligned} &\int d\hat{\mathbf{n}} Y_{l_1 m_1}(\hat{\mathbf{n}}) Y_{l_2 m_2}(\hat{\mathbf{n}}) Y_{l_3 m_3}(\hat{\mathbf{n}}) \\ &= \sqrt{\frac{(2l_1+1)(2l_2+1)(2l_3+1)}{4\pi}} \begin{pmatrix} l_1 & l_2 & l_3 \\ m_1 & m_2 & m_3 \end{pmatrix} \begin{pmatrix} l_1 & l_2 & l_3 \\ 0 & 0 & 0 \end{pmatrix}. \end{aligned} \tag{3.6}$$

Because $l_3 = 1$ for each term in Eq. (3.5), the triangle inequalities obeyed by the 3j symbols give that the only nonzero terms in Eq. (3.5) are $l' = l$ or $l' = l \pm 1$. For these simple cases, the 3j symbols can be evaluated explicitly. Then it is straightforward to derive

$$\left\langle \tilde{a}^*_{l+1\, m\pm1} \tilde{a}_{lm} \right\rangle = \mp \frac{1}{\sqrt{2}} A_\pm \left(C_l + C_{l+1}\right) \sqrt{\frac{(l \pm m + 2)(l \pm m + 1)}{(2l+3)(2l+1)}}, \tag{3.7}$$

$$\left\langle \tilde{a}^*_{l+1\, m} \tilde{a}_{lm} \right\rangle = A_z \left(C_l + C_{l+1}\right) \sqrt{\frac{(l - m + 1)(l + m + 1)}{(2l+3)(2l+1)}}. \tag{3.8}$$

These off-diagonal correlations between multipole coefficients with different l values are zero for an isotropic sky. This result was previously found by [79], and represents a special case of the bipolar spherical harmonic formalism [37].

It is now simple to construct estimators for the components of $\mathbf{A}$ from products of multipole coefficients in a map. Using $A_x = \sqrt{2}\mathrm{Re}A_+$ and $A_y = \sqrt{2}\mathrm{Im}A_+$, we obtain the following estimators:

$$[A_x]_{lm} \simeq \frac{-2}{C_l + C_{l+1}} \sqrt{\frac{(2l+3)(2l+1)}{(l+m+2)(l+m+1)}} \left(\mathrm{Re}\, \tilde{a}_{l+1\, m+1} \mathrm{Re}\, \tilde{a}_{lm} + \mathrm{Im}\, \tilde{a}_{l+1\, m+1} \mathrm{Im}\, \tilde{a}_{lm}\right), \tag{3.9}$$

$$[A_y]_{lm} \simeq \frac{-2}{C_l + C_{l+1}} \sqrt{\frac{(2l+3)(2l+1)}{(l+m+2)(l+m+1)}} \left(\mathrm{Re}\,\tilde{a}_{l+1\,m+1}\mathrm{Im}\,\tilde{a}_{lm} - \mathrm{Im}\,\tilde{a}_{l+1\,m+1}\mathrm{Re}\,\tilde{a}_{lm}\right), \tag{3.10}$$

$$[A_z]_{lm} \simeq \frac{1}{C_l + C_{l+1}} \sqrt{\frac{(2l+3)(2l+1)}{(l+m+1)(l-m+1)}} \left(\mathrm{Re}\,\tilde{a}_{l+1\,m}\mathrm{Re}\,\tilde{a}_{lm} + \mathrm{Im}\,\tilde{a}_{l+1\,m}\mathrm{Im}\,\tilde{a}_{lm}\right). \tag{3.11}$$

where $\tilde{a}_{lm}$'s are calculated from a given (real or simulated) map and C_l's are estimated from the harmonic coefficients of the isotropic map $C_l = (2l+1)^{-1}\sum|a_{lm}|^2$. We argue that for small values of the dipole vector $\mathbf{A}$ and (more important) for a nearly full-sky map $\sum|\tilde{a}_{lm}|^2 \to \sum|a_{lm}|^2$. This assumption has been tested for the kinematic dipole modulation induced in the CMB due to our proper motion, showing that the bias on the estimated power spectrum is much smaller than the cosmic variance error for nearly full-sky surveys [44]. Such estimators, derived under the constraint of constant dipole modulation, can be safely used for the general case of a scale-dependent dipole vector $\mathbf{A}$ by assuming that $\mathbf{A}(l) \simeq \mathbf{A}(l+1)$. This requirement is trivially satisfied by a small and monotonically decreasing function $\mathbf{A}(l)$.

To compute the variance of these estimators, assume a full-sky microwave background map which is dominated by cosmic variance; the Planck maps are a good approximation to this ideal. Then a_{lm} is a Gaussian random variable with variance $\sigma_l^2 = C_l$. The real and imaginary parts are also each Gaussian distributed, with a variance half as large. The product $x = \mathrm{Re}\,\tilde{a}_{l+1\,m+1}\mathrm{Re}\,\tilde{a}_{lm}$, for example, will then have a product normal distribution with probability density

$$P(x) = \frac{2}{\pi\sigma_l\sigma_{l+1}} K_0\left(\frac{2|x|}{\sigma_l\sigma_{l+1}}\right) \tag{3.12}$$

with variance $\sigma_x^2 = \sigma_l^2\sigma_{l+1}^2/4$, where $K_0(x)$ is a modified Bessel function. By the central limit theorem, a sum of random variables with different variances will tend to a normal distribution with variance equal to the sum of the variances of the random variables; in practice the sum of two random variables each with a product normal distribution will be very close to normally distributed, as can be verified numerically from Eq. (3.12). Therefore

we can treat the sums of pairs of $\tilde{a}_{lm}$ values in Eqs. (3.9) to (3.11) as normal variables with variance $\sigma_l^2\sigma_{l+1}^2/2$, and obtain the standard errors for the estimators as

$$\begin{aligned}[\sigma_x]_{lm} &= [\sigma_y]_{lm} \\ &\simeq \sqrt{\frac{(2l+3)(2l+1)}{2(l+m+2)(l+m+1)}},\end{aligned} \tag{3.13}$$

$$[\sigma_z]_{lm} \simeq \frac{1}{2}\sqrt{\frac{(2l+3)(2l+1)}{2(l+m+1)(l-m+1)}}, \tag{3.14}$$

with the approximation $C_{l+1} \simeq C_l$.

For a sky map with cosmic variance, each estimator of the components of $\mathbf{A}$ for a given value of l and m will have a low signal-to-noise ratio. Averaging the estimators with inverse variance weighting will give the highest signal-to-noise ratio. Consider such an estimator for a component of $\mathbf{A}$ which average all of the multipole moments between $l = a$ and $l = b$:

$$[A_x] \equiv \sigma_x^2 \sum_{l=a}^{b} \sum_{m=-l}^{l} \frac{[A_x]_{lm}}{[\sigma_x]_{lm}^2}, \tag{3.15}$$

$$[A_y] \equiv \sigma_y^2 \sum_{l=a}^{b} \sum_{m=-l}^{l} \frac{[A_y]_{lm}}{[\sigma_y]_{lm}^2}, \tag{3.16}$$

$$[A_z] \equiv \sigma_z^2 \sum_{l=a}^{b} \sum_{m=0}^{l} \frac{[A_z]_{lm}}{[\sigma_z]_{lm}^2}, \tag{3.17}$$

which have standard errors of

$$\begin{aligned}\sigma_x &= \sigma_y \\ &\equiv \left[\sum_{l=a}^{b} \sum_{m=-l}^{l} [\sigma_x]_{lm}^{-2}\right]^{-1/2} \\ &= \left[\frac{2}{3}(b+a+2)(b-a+1)\right]^{-1/2},\end{aligned} \tag{3.18}$$

$$\begin{aligned}\sigma_z &\equiv \left[\sum_{l=a}^{b} \sum_{m=0}^{l} [\sigma_z]_{lm}^{-2}\right]^{-1/2} \\ &= \left[\frac{4(b-a+1)\left[a(2b+3)(a+b+4)+(b+2)(b+3)\right]}{3(2a+1)(2b+3)}\right]^{-1/2}.\end{aligned} \tag{3.19}$$

The sum over m for the z estimator and error runs from 0 instead of $-l$ because $[A_z]_{l-m} = [A_z]_{lm}$, but the values are distinct for the x and y estimators.

While the Cartesian components are real Gaussian random variables, such that for isotropic models $\langle [A_x] \rangle = \langle [A_y] \rangle = \langle [A_z] \rangle = 0$, the amplitude of $\mathbf{A}$ is not Gaussian distributed. Instead, it is described by a chi-square distribution with 3 degrees of freedom, which implies $\langle |\mathbf{A}|^2 \rangle \neq 0$ and $p(|\mathbf{A}|^2 = 0) = 0$, even for an isotropic sky. For this reason, we consider the properties of the dipole vector $\mathbf{A}$ as function of the multipole, considering each Cartesian component separately.

3.3 SIMULATIONS AND ANALYSIS PIPELINE

The estimators in Eqs. (3.9) - (3.11) are clearly unbiased for the case of full-sky CMB map. However, residual foreground contaminations along the galactic plane as well as point sources may cause a spurious dipole modulation signal, which can be interpreted as cosmological. Such highly contaminated regions can be masked out, at the cost of breaking the statistical isotropy of the CMB field and inducing off-diagonal correlations between different modes. The effect of the mask, which has a known structure, can be characterized and removed.

3.3.1 Characterization of the Mask

For a masked sky the original a_{lm} are replaced with their masked counterparts:

$$\overline{a}_{lm} = \int \mathbf{d}\Omega \Theta(\hat{\mathbf{n}}) W(\hat{\mathbf{n}}) Y^*_{lm} \tag{3.20}$$

where $W(\hat{\mathbf{n}})$ is the mask, with $0 \leq W(\hat{\mathbf{n}}) \leq 1$. In this case, Eq. (3.4) does not hold, meaning that even for a statistical isotropic but masked sky the estimators in Eq. (3.9)-(3.11) will have an expectation value different from zero. This constitutes a bias factor in our estimation of the dipole modulation.

If we expand Eqs. (3.9)–(3.11) using the definition of the harmonic coefficients in Eq. (3.5), it is clear that if a primordial dipole modulation is present, the mask transfers power between different Cartesian components. Under the previous assumption $\mathbf{A}(l) \simeq \mathbf{A}(l+1)$, the Cartesian components $i, j = x, y, z$ of the dipole vector can be written as

$$[\overline{A}_j]_{lm} = \mathbf{\Lambda}_{ji,lm} A_{i,l} + M_{j,lm} \tag{3.21}$$

where $[\overline{A}_j]_{lm}$ is the estimated dipole vector for the masked map, and $\mathbf{\Lambda}_{ji,lm}$ and $M_{j,lm}$ are Gaussian random numbers determined by the $\overline{a}_{lm}$, so dependent only on the geometry of the mask. For unmasked skies, these two quantities satisfy $\langle \mathbf{\Lambda}_{ji,lm} \rangle = \delta_{ij}$ and $\langle M_{j,lm} \rangle = 0$, ensuring that the expectation value of our estimator converges to the true value.

Using Eq. (3.21), we can define a transformation to recover the true binned dipole vector from a masked map:

$$[A_i] = \mathbf{\Lambda}_{ji}^{-1} ([\overline{A}_j] - M_j) \tag{3.22}$$

where $[\overline{A}_j]$ is the binned dipole vector estimated from a map, and $\mathbf{\Lambda}_{ji}$ and M_j are the expectation values of $\mathbf{\Lambda}_{ji,lm}$ and $M_{j,lm}$, binned using the prescription in Eqs. (3.15)–(3.17). For each Cartesian component we divide the multipole range in 19 bins with uneven spacing, $\Delta l = 10$ for $2 \leq l \leq 100$, $\Delta l = 100$ for $101 \leq l \leq 1000$. For a given mask, the matrix $\mathbf{\Lambda}_{ji}$ and the vector M_j can be computed by using simulations of isotropic masked skies. We use an ensemble of 2000 simulations, and we adopt the apodized `Planck U73` mask, following the procedure adopted by PLK13 for the hemispherical power asymmetry analysis. For the rest of this work, all estimates of the dipole vector are corrected for the effect of the mask using Eq. (3.22).

3.3.2 Simulated Skies

We generate 2000 random masked skies for both isotropic and dipole modulated cases. For the latter, we assume an scale-independent model with amplitude $|\mathbf{A}| = 0.07$, along the direction in galactic coordinates $(l, b) = (220°, -20°)$. We adopt a resolution corresponding to the `HEALPix`[1] [34] parameter `NSIDE` $= 2048$, and we include a Gaussian smoothing of `FWHM`

[1] `http://healpix.sourceforge.net/`

$= 5'$ to match the resolution of the available maps. The harmonic coefficients $\tilde{a}_{lm}$ are then rescaled by $\sqrt{\tilde{C}_l}$, where the power spectrum is calculated directly from the masked map. These normalized coefficients (for both isotropic and dipole modulated cases) are then used to estimate the components of the dipole vector.

These simulations also serve the purpose of estimating the covariance matrix $\mathbf{C}$. From Eqs. (3.9)-(3.11), we expect different Cartesian components to be nearly uncorrelated, even for models with a non-zero dipole modulation, for full-sky maps. We confirm this numerically with simulations of unmasked skies. For masked skies, Fig. 3.1 shows the covariance matrices. The left panel shows the case for isotropic skies with no dipole modulation. The presence of the mask induces correlations between multipole bins at scales $100 \lesssim l \lesssim 500$, and also between the largest scales $l \lesssim 40$ with all the other multipole bins. However, because of the apodization applied to the mask, the correlation between bins never exceeds 25%. For comparison, we also show the difference between the correlation matrices for the case of dipole modulated and isotropic skies (right panel). This is consistent with random noise, which demonstrates that the covariance matrix does not depend significantly on the amplitude of the dipole modulation.

3.3.3 Bias Estimates

We determine the mean bias in reconstructing the dipole modulation vector $\mathbf{A}$ from a masked sky by computing the mean value of all three Cartesian components reconstructed from 2000 simulations, for both isotropic and dipole-modulated skies. In both cases, the residual bias vector has components $A_i > 0$, with an amplitude of the first bin of each Cartesian component below 6×10^{-3}. For the isotropic case, the amplitude of the bias is strongly decreasing with multipole ($|A(l = 60)| = 3.8 \times 10^{-4}$), corresponding to 0.5% to 2% of the cosmic variance error for the entire multipole range considered. Therefore, the analysis procedure on masked skies does not introduce a statistically any significant signal which could be mistaken for dipole modulation.

In the case of dipole-modulated simulations with dipole amplitude $A = 0.07$ consistent with PLK13, the amplitude of the bias for each Cartesian component is a constant for all

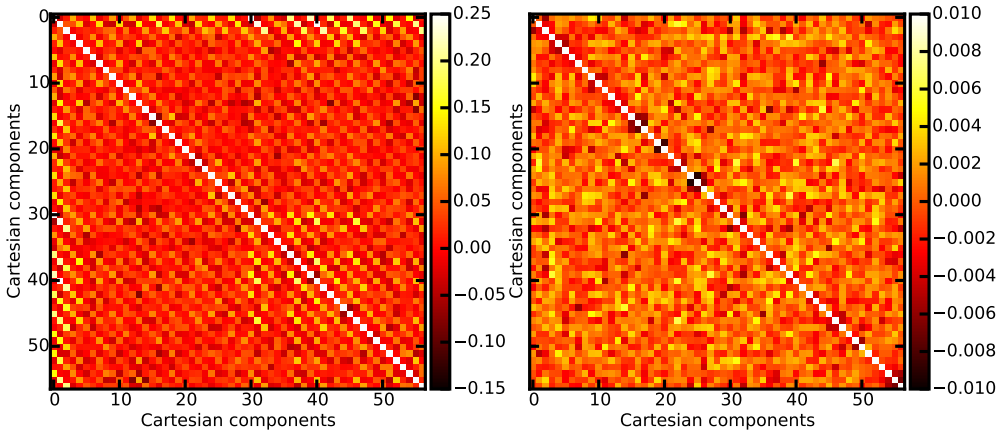

Figure 3.1: Correlation matrices for the Cartesian components of the dipole vector. These matrices are estimated using 2000 random simulated skies masked with the apodized Planck U73 mask. The ordering of the components follows the convention defined for the dipole vector. (Left panel) Isotropic skies ($\mathbf{A}$=0). (Right panel) Difference between the correlation matrices for modulated skies, generated using a constant dipole vector across multipoles of magnitude $|\mathbf{A}| = 0.07$ and direction $(l, b) = (220°, -20°)$, and isotropic skies.

multipoles. This indicates that the bias follows the underlying model, and the determination of the scale dependence of the true dipole vector will not be affected by such a bias. For this specific case, the amplitude is always $\leq 0.8\sigma$ when compared to the cosmic variance, specifically $\leq 0.1\sigma$ for $l \leq 100$. However, this simulated case is unrealistic. We do not expect such a big amplitude for the dipole vector at small scales, so the simulated case overestimates the actual bias.

3.4 MICROWAVE SKY DATA

We consider a suite of six different foreground-cleaned microwave background temperature maps:[2]: SMICA, NILC, COMMANDER-Ruler H and SEVEM from the first Planck data release [73], and two others processed with the LGMCA[3] component separation technique by [12]. The LGMCA-PR1 and LGMCA-WPR1 are based on Planck data only and Planck+WMAP9 data respectively, allowing a non trivial consistency test between these two experiments. Each of these maps uses a somewhat different method for separating the microwave background component from foreground emission, allowing us to quantify any dependence on the component separation procedure.

Asymmetric beams and inhomogeneous noise may create a systematic dipolar modulation in the sky. In order to test this possibility, we analyze the 100 publicly available FFP6 single-frequency simulated maps released by the Planck team. Specifically, we process the simulations for the 100, 143 and 217 GHz channels with our analysis code. The maximum likelihood analysis shows a bias on small scales, although the values are always less than 0.6 times the cosmic variance for each multipole bin. Considering only the first 15 bins ($l_{\rm max} = 600$) gives a result consistent with the isotropic case, with a p-value larger than 0.1. The source of the small-scale bias is not yet known, but we simply ignore multipoles $l > 600$ in the present analysis of Planck data.

3.5 RESULTS

Fig. 3.2 shows the measured values of the Cartesian components of the dipole vector, using the SMICA map. Similar results are found for the other foreground-cleaned maps, and a direct comparison is shown in Sec. 3.5.1. Fig. 3.3 displays the amplitude of the dipole vector compared with the mean value (black dashed line) obtained from isotropic simulations; as pointed out in Sec. **??**, the expectation value of the amplitude of the dipole vector is different

[2] http://wiki.cosmos.esa.int/planckpla/index.php/Main_Page
[3] http://www.cosmostat.org/product/lgmca_cmb/

from zero even for the isotropic case.

The data clearly shows two important features:

(i) The amplitudes of the components of the estimated dipole vector are decreasing functions of the multipole ℓ.

(ii) The x and y components have a negative sign, which persists over a wide range of multipoles; the z component is consistent with zero. This indicates that the vector is pointing in a sky region ($180^\circ < l < 270^\circ, b \simeq 0$), in agreement with previous analyses.

We further characterize these basic results in the remainder of this Section.

3.5.1 Geometrical Test

First, we test how likely the observed geometrical configuration of the dipole vector is in an isotropic universe. To achieve this goal, we need to define a quantity which preserves the information on the direction of the dipole vector (i.e. statistics linear in the variables A_i). In addition, the Cartesian components have to be weighted by the cosmic variance, ensuring that our statistics is not dominated by the first bins. Therefore, we define the following quantity

$$\alpha = \sum_{i=1}^{3N} (\mathbf{C}^{-1})_{ij} [A]_{j=1,\dots,3N} \tag{3.23}$$

where $(\mathbf{C}^{-1})_{ij}$ are the components of the inverse of the covariance matrix calculated in Sec. 3.3.2, and $[A]_{j=1,\dots,3N}$ are the three Cartesian components of the binned dipole vector (up to the $N^{\rm th}$ bin) estimated either from a simulated map of measured data. For an isotropic universe, we expect the three Cartesian components to sum up to zero, such that $\langle \alpha \rangle = 0$ for any choice of $l_{\rm max}$. This will not be the case if the underlying model is not isotropic (i.e. the expectation values of the Cartesian components are different from zero). In Fig. 3.4, we plot the values of the α parameter as function of the maximum multipole considered in the analysis l_{max}, rescaled by the standard deviation $\sigma(\alpha)$ determined from the simulations of isotropic skies. The left panel shows the comparison between the CMB data for all 6 foreground-cleaned maps, and the simulations for the isotropic case. The measured rescaled α parameter has a value that is discrepant from $\alpha = 0$ at a level of $2\sigma \lesssim \alpha < 3\sigma$. This discrepancy is maximized for $l \lesssim 60 - 70$, which corresponds to what has been previously

probed by PLK13.

The right panel of Fig. 3.4 compares the measured signal with simulations of dipole modulated skies, using the covariance matrix $\mathbf{C}$ calculated from the anisotropic simulations. This test confirms that the signal averaged over multipoles $\lesssim 60-70$ is consistent with the model proposed by PLK13 (assumed in our anisotropic simulations). However, the results are not consistent with a scale-independent dipole modulation, and the amplitude of the dipole modulation vector must be strongly suppressed at higher multipoles.

3.5.2 Model Fitting

Consider a simple power-law model for the dipole modulation defined by 4 parameters (in this section we indicate multipoles with the symbol ℓ, and for the galactic longitude we use l):

$$A_x^{\rm th} = A\Big(\frac{\ell}{60}\Big)^n \cos b \cos l, \tag{3.24}$$

$$A_y^{\rm th} = A\Big(\frac{\ell}{60}\Big)^n \cos b \sin l, \tag{3.25}$$

$$A_z^{\rm th} = -A\Big(\frac{\ell}{60}\Big)^n \sin b, \tag{3.26}$$

where A is the amplitude of the dipole vector at the pivot scale of $\ell = 60$, n is the spectral index of the power law, b is the galactic latitude, and ℓ is the galactic longitude. We use a Gaussian likelihood $\mathcal{L}$, such that

$$\ln\mathcal{L} = -\frac{1}{2}\chi^2 = -\frac{1}{2}([A_i]-[A_i]^{\rm th})^{\rm T}(\mathbf{C}^{-1})_{ij}([A_j]-[A_j]^{\rm th}) \tag{3.27}$$

where $[A_i]$ are the estimated components from the Planck SMICA map, $[A_i]^{\rm th}$ are the components of the assumed model properly binned using Eqs. (3.15)-(3.17), and C is the covariance matrix for a dipole-modulated sky displayed in Fig. 3.1. The parameter space is explored using the Markov chain Monte Carlo sampler `emcee` [32], assuming flat priors over the ranges $\{A, n\} = \{[0,1],[-2,2]\}$. Table 3.1, displays the results for different thresholds of $\ell_{\rm max}$.

In the restricted case considering only low multipoles $l < 60$ and a flat spectrum $n = 0$, our best-fit model agrees at the 1σ level with previous analysis by PLK13, for both amplitude and direction.

If n is allowed to vary, the amplitude A of the dipole vector at the pivot scale of 60, as well as the spectral index n, are perfectly consistent for three different $l_{\rm max}$ thresholds. The amplitude is different from the isotropic case $A = 0$ at a level of 2σ, and the scale-invariant case $n = 0$ with $l_{\rm max} = 400$ is excluded at greater than 3σ significance. The value of the galactic longitude l is stable to a very high degree, whereas the value of galactic latitude b indicates (although not statistically significant) a migration of the pointing from the southern hemisphere to the northern one. This is expected due to the effect of the kinematic dipole modulation induced by the proper motion of the solar system with respect to the microwave background rest frame [80, 17, 52]. This effect has been detected by Planck [77], and results in a dipole modulation in the direction $(l, b) = (264^\circ, 48^\circ)$ detectable at high ℓ.

The dipole model is a better fit to the data than isotropic models. Both the Aikake information criterion (AIC) and the Bayes information criteron (BIC) [55] show sufficient improvement in the fit to justify the addition of four extra parameters in the model. In the specific case of the AIC, the dipole model is always favored. The improvement is calculated by the relative likelihood of the isotropic model with respect to the dipole modulated case. This is defined as $\exp((\mathrm{AIC}_{\rm min} - \mathrm{AIC}_{\rm A=0})/2)$, where the AIC factor is corrected for the finite sample size, and it corresponds to 0.48, 0.083, 0.13, 0.18, 0.013, and 0.011 for the models considered in Table 3.1. In the case of the BIC, the corresponding values are $BIC_{\rm min} - BIC_{A=0} = 0.5$; 0.4; 1.0; 2.1; 2.8, and 2.8. The BIC indicates that the dipole modulation is favored only for the cases with $\ell_{\rm max} > 400$, where the parameters are better constrained. According to Ref. [47], the improvement, even though positive, is not strong because $-6 < BIC_{\rm min} - BIC_{A=0} < -2$.

For the dipole-modulated model, the value of χ^2 is substantially lower than the degrees of freedom. This suggests that either the error bars are overestimated or the data points have correlations which have not been accounted for in the simple dipole model. Since the errors are mostly due to cosmic variance on the scales of interest, the error bars cannot have been significantly overestimated. Therefore, our results may point to additional correlations in the microwave temperature pattern beyond those induced by a simple dipole modulation

of Gaussian random anisotropies. The correlations are unlikely to be due to foregrounds, since the results show little dependence on different foreground removal techniques.

3.6 DISCUSSION

The microwave sky seems to exhibit a departure from statistical isotropy, due to half the sky having slightly more temperature fluctuation power than the other half. This work shows that the temperature anisotropies are consistent with a dipolar amplitude modulation, which induces correlations with multipole coefficients with ℓ values differing by one. At angular scales of a few degrees and above, the correlations define a dipole direction which corresponds to the orientation of the previously known hemispherical power asymmetry, while at smaller scales the direction migrates to that of the kinematic dipole. Our results show that a dipole modulation is phenomenologically a good description of the power asymmetry, but that the modulation must be scale dependent, becoming negligible compared to the kinematic dipole correlations [52, 77] on angular scales well below a degree.

The statistical significance of these multipole correlations is between 2σ and 3σ compared to an isotropic sky, with the error dominated by cosmic variance. The maximum signal appears at scales $l \lesssim 70$ as seen previously by PLK13. We also find an unusually low scatter in the dipole component estimates as a function of scale, given the cosmic variance of an unmodulated Gaussian random field, suggesting that the microwave temperature sky may have additional correlations not captured by this simple model.

On the largest scales of the universe, simple models of inflation predict that the amplitude of any dipole modulation due to random perturbations in a statistically isotropic universe should be substantially smaller than that observed. This departure from statistical isotropy may require new physics in the early Universe. One possible mechanism is a long-wavelength mode of an additional field which couples to the field generating perturbations [26, 24, 25, 21, 60, 23, 85, 57, 64, 56, 62, 22, 14, 18, 50, 63, 46, 58, 19, 65, 68, 5, 29, 67]. If the mode has a wavelength longer than the current Hubble length, an observer sees its effect as a gradient. The field gradient modulates background physical quantities such as the effective inflaton

potential or its slow-roll velocity. The required coupling between long and short wavelength modes can be accomplished in the context of squeezed-state non-Gaussianity [68, 5, 29, 67]. This mechanism requires a non-trivial scale-dependent non-Gaussianity.

Apart from the hypothesis of new physics, foreground contamination and instrumental systematics can break the statistical isotropy of the microwave background temperature map. However, these possibilities can be tested with the available data. Our estimates of the Cartesian components of the dipole vector, as functions of angular scale, are consistent for different foreground-cleaned temperature maps. The masking adopted in this analysis removes most contaminations from diffuse galactic emission and point sources, and our analysis procedure controls possible biases introduced by this procedure. In addition, realistic instrument simulations provided by the Planck Collaboration exclude instrumental effects as the source of the observed isotropy breaking at the angular scales of interest. While this work was in preparation, the Planck team made available the results of a similar analysis using the 2015 temperature maps (PLK15) [71]. Our estimates of the amplitude and direction of the dipole modulation vector on large scales ($\ell_{max} = 60$) are consistent with PLK15 analysis based on bipolar spherical harmonics. The PLK15 analysis does not provide a constraint on the scale dependency, although it shows (as for the PLK13 analysis) that the amplitude must decrease at higher multipoles. PLK15 shows that the amplitude of the dipole vector differs from the isotropic case at a level of $2\sigma - 3\sigma$ when calculated in cumulative multipole bins $[2, \ell_{max}]$ for ℓ_{max} up to 320. This result can be compared with our geometrical test, for which similar results are found.

Additional tests of the dipole modulation will be possible with high-sensitivity polarization maps covering significant portions of the sky (see, e.g., [15, 49]). In the standard inflationary cosmology, microwave polarization and temperature are expected to be only partially correlated, giving an additional independent probe of a dipole modulation; a cosmic-variance limited polarization map will likely double the statistical significance of the signal studied here. Gravitational lensing of the microwave background over large sky regions provides another nearly independent probe which will be realized in the near future. We will consider these possibilities elsewhere. If these probes substantially increase the statistical significance of the dipolar modulation signal, we will be forced into some significant modification to the

inferred physics of the early Universe.

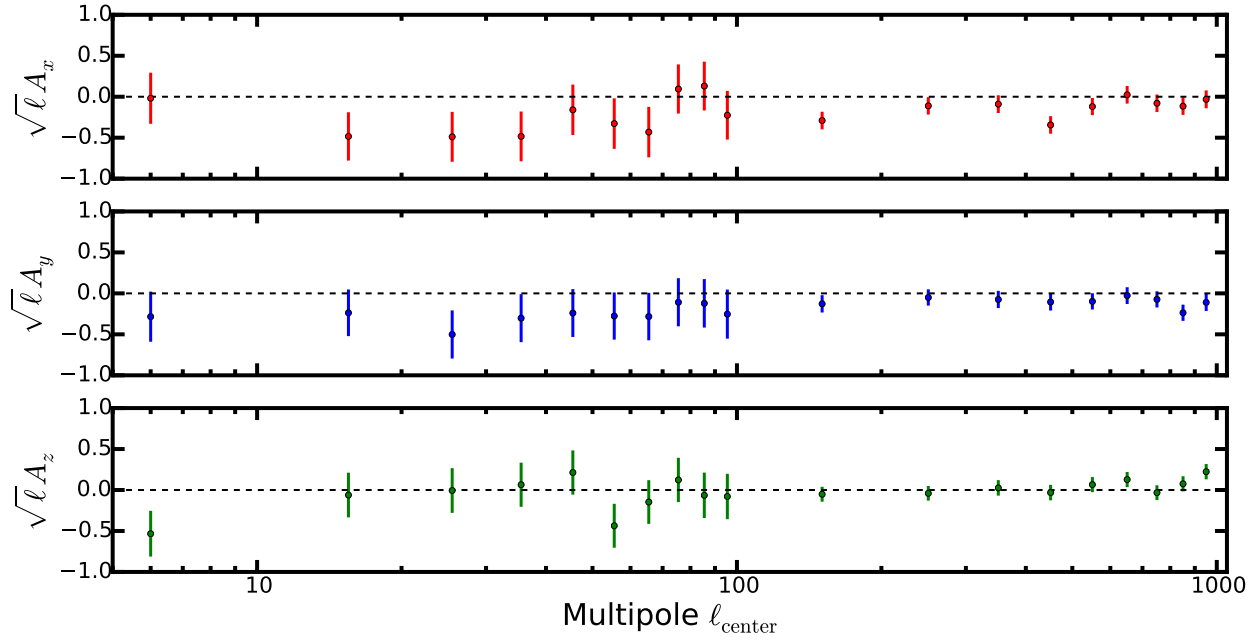

Figure 3.2: Measured Cartesian components of the dipole vector from the SMICA Planck map as a function of the central bin multipole $\ell_{\rm center}$. The amplitudes are multiplied by $\sqrt{\ell}$ to enhance visibility of the signal at higher multipoles. The 1σ errors are the square roots of the covariance matrix diagonal elements. Data at $\ell > 600$ is not used in our statistical analyses.

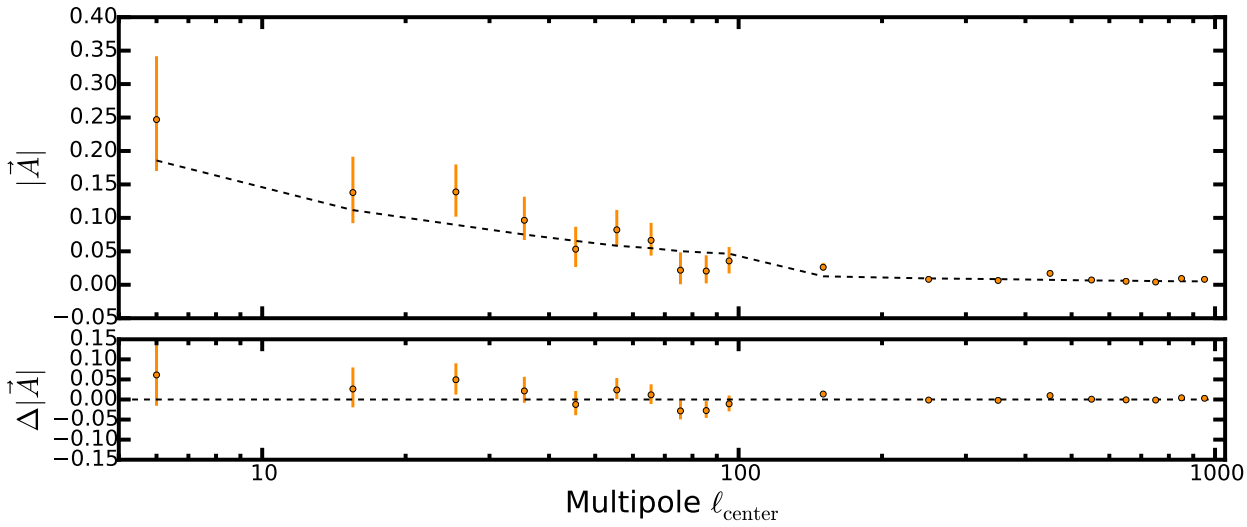

Figure 3.3: Measured amplitude of the dipole vector from the SMICA Planck map. The black dashed line shows the model for the statistical isotropic case $\mathbf{A}$=0. The 1σ errors are estimated from the $16^{\rm th}$ and $84^{\rm th}$ percentiles of the distribution of the dipole vector amplitudes, calculated from sky simulations processed the same way as the data.

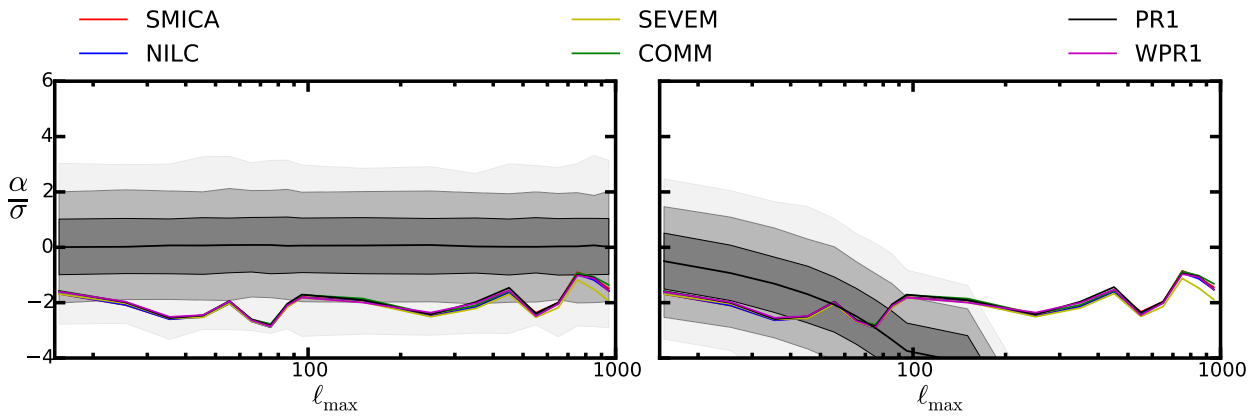

Figure 3.4: The $\alpha-$parameter from Eq. (3.23), scaled by the standard deviation $\sigma(\alpha)$, as function of the maximum multipole considered $\ell_{\rm max}$. The colored solid lines are the results from CMB data, showing remarkable consistency between different foreground cleaning methods. (Left panel) The shaded bands are estimated using simulations of isotropic masked skies. The distribution α-parameter is Gaussian with $\langle\alpha\rangle = 0$. (Right panel) The shaded bands are estimated using simulations of dipole modulated masked skies. The dipole modulation model is $A = 0.07$, $(l, b) = (220^\circ, -20^\circ)$. The confidence regions (colored band) are estimated using percentiles, such that $\pm1\sigma = [15.87^{\rm th}/\sigma(\alpha), 84.13^{\rm rd}/\sigma(\alpha)]$, $\pm2\sigma = [2.28^{\rm th}/\sigma(\alpha), 97.72^{\rm nd}/\sigma(\alpha)]$ and $\pm3\sigma = [0.13^{\rm rd}/\sigma(\alpha), 99.87^{\rm th}/\sigma(\alpha)]$.

$\ell_{\rm max}$	A	n	$b[^\circ]$	$l[^\circ]$	$\chi^2_{\rm min}(\nu)$	$\chi^2_{A=0}(\nu)$
60	$0.063^{+0.028}_{-0.030}$	$-$	-10^{+21}_{-21}	$+218^{+24}_{-24}$	10.3 (15)	19.5 (18)
200	$0.034^{+0.014}_{-0.016}$	$-0.54^{+0.38}_{-0.22}$	-7^{+16}_{-16}	$+211^{+19}_{-19}$	16.4 (29)	30.8 (33)
300	$0.029^{+0.012}_{-0.014}$	$-0.68^{+0.26}_{-0.19}$	-11^{+18}_{-16}	$+211^{+20}_{-20}$	18.1 (32)	31.4 (36)
400	$0.027^{+0.012}_{-0.014}$	$-0.74^{+0.22}_{-0.18}$	-9^{+19}_{-18}	$+212^{+22}_{-21}$	19.3 (35)	31.9 (39)
500	$0.031^{+0.012}_{-0.013}$	$-0.61^{+0.23}_{-0.15}$	-4^{+13}_{-13}	$+207^{+16}_{-16}$	22.5 (38)	40.2 (42)
600	$0.031^{+0.011}_{-0.012}$	$-0.64^{+0.19}_{-0.14}$	-1^{+13}_{-14}	$+209^{+16}_{-15}$	23.9 (41)	41.9 (45)

Table 3.1: Best-fit values of the amplitude A, spectral index n and direction angles (l, b) for the dipole vector, as function of the maximum multipole $\ell_{\rm max}$. The best fit values are corresponds to the $50^{\rm th}$ percentile of the posterior distribution marginalized over the other parameters. The errors corresponds to the $16^{\rm th}$ and $84^{\rm th}$ percentiles. For the first case, we consider a model with spectral index $n = 0$ and $\ell_{\rm max} = 60$, which can be compared with PLK13 findings. Values of the χ^2 corresponding to the best fit model, as well as to the isotropic case, are also displayed with corresponding number of degrees of freedom ν.

4.0 CONCLUSION

The success of the Standard Model of Cosmology is evident in its becoming of the dominant paradigm of the current era of cosmology. The precise agreement between observation and theory exceeds what cosmologists had wished for in pre-CMB era. Whether considering WMAP/Planck data alone, or in combination with other cosmological data, overall the Standard Model gives the most satisfying description. In this regard, hardly any other model is more compelling. However, it should also be acknowledged that the Standard Model is perhaps not the final story: There remain questions unanswered, predications unverified, and limits to be pushed towards the unknowns, all of which are the factors that make anomalies interesting. In the investigation of possible deviations from the Standard Model lies the clues for new physics, and the efforts made toward this direction lead to the works in this thesis.

The cosmological constant problem is one of the outstanding problems of modern physics. A possible venue to study dark energy is via the late-ISW effect, of which unfortunately the small amplitude imposes observational challenges. Its strongest detection comes from the aperture photometry on stacked CMB features at the locations of known superclusters and supervoids seen in the Sloan Digital Sky Survey [35], which is claimed to be 3σ deviated from the expectation value. Our analysis brings this tension down to 2.5σ by including the correlations between the late-ISW signal and other sources of CMB temperature anisotropies, which mildly increases the theoretical mean signal while also increasing the statistical uncertainty. Subsequent studies carried out in Ref. [53] used a new catalogue from the CMASS survey, and showed that ISW detections with the stacking protocol strongly depend on the properties of the tracer population and the void finder. The analysis from Planck DR2 [76], in which the Planck polarization data is used to explore further the origin of the stacking signal, indicates a secondary nature of the stacking signal. At current stage, therefore, it

remains an open question whether such anomaly is physical, coincidence, or post-hoc statistics, though a failure in reproducing the same statically significance in the CMASS catalog indicates a direction toward the latter two explanations.

The second anomaly discussed in this thesis—the hemispherical power asymmetry—has a longer history of disputation. It is brought into sight ever since the first data release of WMAP [28]. Despite WMAP team's claim that after a posteriori choices are carefully removed from the analysis, the anomalous dipole power asymmetry is not statistically significant [8], it remains a topic being discussed. Our analysis concludes that the observed dipole asymmetry is unlikely at $2\sigma - 3\sigma$ level as compared to an isotropic case, and our estimates of the amplitude and direction of the dipole modulation vector on large scales ($\ell_{max} = 60$) are consistent with PLK15 analysis based on bipolar spherical harmonics. As a step further, we quantify the scale dependency by fitting a simple power-law. Though such choice is purely phenomenological, our approach can be adapted for examining the dipole modulation of other cosmological fields such as CMB polarization and CMB lensing.

Looking into the future, upcoming optical surveys like Skymapper [48], DES [84], DESI [54], and LSST [59] promise a substantial expansion in the census of voids and clusters suitable for late-ISW peak analysis; microwave polarization and temperature are expected to be only partially correlated in the standard inflationary cosmology, giving an additional independent probe of a dipole modulation. Gravitational lensing of the microwave background over large sky regions provides another nearly independent probe which will be realized in the near future. With the increasing flow of data, many possibilities lay ahead on the quest for an understanding of the physics of and beyond the Standard Model.

BIBLIOGRAPHY

[1] J. K. Adelman-McCarthy et al. The Sixth Data Release of the Sloan Digital Sky Survey. *ApJS*, 175:297–313, 2008.

[2] S. Adhikari. Local variance asymmetries in Planck temperature anisotropy maps. *Mon. Not. R. Astron Soc.*, 446:4232–4238, 2015.

[3] S. Aiola, A. Kosowsky, and B. Wang. Gaussian approximation of peak values in the integrated Sachs-Wolfe effect. Phys. Rev. D, 91(4):043510, February 2015.

[4] S. Aiola, B. Wang, A. Kosowsky, T. Kahniashvili, and H. Firouzjahi. Microwave background correlations from dipole anisotropy modulation. Phys. Rev. D, 92(6):063008, September 2015.

[5] A. Akbar Abolhasani, S. Baghram, H. Firouzjahi, and M. H. Namjoo. Asymmetric Sky from the Long Mode Modulations. 2013.

[6] Y. Akrami, Y. Fantaye, A. Shafieloo, H. K. Eriksen, F. K. Hansen, A. J. Banday, and K. M. Górski. Power Asymmetry in WMAP and Planck Temperature Sky Maps as Measured by a Local Variance Estimator. *Astrophys. J. Lett.*, 784:L42, 2014.

[7] L. Amendola, R. Catena, I. Masina, A. Notari, M. Quartin, and C. Quercellini. Measuring our peculiar velocity on the CMB with high-multipole off-diagonal correlations. *J. Cosmol. Astropart. Phys.*, 7:27, 2011.

[8] C. L. Bennett, R. S. Hill, G. Hinshaw, D. Larson, K. M. Smith, J. Dunkley, B. Gold, M. Halpern, N. Jarosik, A. Kogut, E. Komatsu, M. Limon, S. S. Meyer, M. R. Nolta, N. Odegard, L. Page, D. N. Spergel, G. S. Tucker, J. L. Weiland, E. Wollack, and E. L. Wright. Seven-year Wilkinson Microwave Anisotropy Probe (WMAP) Observations: Are There Cosmic Microwave Background Anomalies? ApJS, 192:17, February 2011.

[9] C. L. Bennett, D. Larson, J. L. Weiland, N. Jarosik, G. Hinshaw, N. Odegard, K. M. Smith, R. S. Hill, B. Gold, M. Halpern, E. Komatsu, M. R. Nolta, L. Page, D. N. Spergel, E. Wollack, J. Dunkley, A. Kogut, M. Limon, S. S. Meyer, G. S. Tucker, and E. L. Wright. Nine-year Wilkinson Microwave Anisotropy Probe (WMAP) Observations: Final Maps and Results. ApJS, 208:20, October 2013.

[10] D. Blas, J. Lesgourgues, and T. Tram. The Cosmic Linear Anisotropy Solving System (CLASS). Part II: Approximation schemes. *JCAP*, 7:34, 2011.

[11] J. Bobin, F. Sureau, J.-L. Starck, A. Rassat, and P. Paykari. Joint Planck and WMAP CMB map reconstruction. *A&A*, 563:A105, 2014.

[12] J. Bobin, F. Sureau, J.-L. Starck, A. Rassat, and P. Paykari. Joint Planck and WMAP CMB map reconstruction. *Astron. Astrophys.*, 563:A105, 2014.

[13] Y.-C. Cai, B. Li, S. Cole, C. S. Frenk, and M. Neyrinck. The integrated Sachs-Wolfe effect in f(R) gravity. *MNRAS*, 439:2978–2989, 2014.

[14] Y.-F. Cai, W. Zhao, and Y. Zhang. Cosmic microwave background power asymmetry from primordial sound speed parameter. Phys. Rev. D, 89(2):023005, 2014.

[15] E. Calabrese, R. Hložek, N. Battaglia, J. R. Bond, F. de Bernardis, M. J. Devlin, A. Hajian, S. Henderson, J. C. Hil, A. Kosowsky, T. Louis, J. McMahon, K. Moodley, L. Newburgh, M. D. Niemack, L. A. Page, B. Partridge, N. Sehgal, J. L. Sievers, D. N. Spergel, S. T. Staggs, E. R. Switzer, H. Trac, and E. J. Wollack. Precision epoch of reionization studies with next-generation CMB experiments. J. Cosmology Astropart. Phys., 8:010, August 2014.

[16] J. E. Carlstrom, P. A. R. Ade, K. A. Aird, B. A. Benson, L. E. Bleem, S. Busetti, C. L. Chang, E. Chauvin, H.-M. Cho, T. M. Crawford, A. T. Crites, M. A. Dobbs, N. W. Halverson, S. Heimsath, W. L. Holzapfel, J. D. Hrubes, M. Joy, R. Keisler, T. M. Lanting, A. T. Lee, E. M. Leitch, J. Leong, W. Lu, M. Lueker, D. Luong-van, J. J. McMahon, J. Mehl, S. S. Meyer, J. J. Mohr, T. E. Montroy, S. Padin, T. Plagge, C. Pryke, J. E. Ruhl, K. K. Schaffer, D. Schwan, E. Shirokoff, H. G. Spieler, Z. Staniszewski, A. A. Stark, C. Tucker, K. Vanderlinde, J. D. Vieira, and R. Williamson. The 10 Meter South Pole Telescope. PASP, 123:568–581, May 2011.

[17] A. Challinor and F. van Leeuwen. Peculiar velocity effects in high-resolution microwave background experiments. Phys. Rev. D, 65(10):103001, May 2002.

[18] Z. Chang, X. Li, and S. Wang. Quadrupole–octopole alignment of CMB related to primordial power spectrum with dipolar modulation in anisotropic spacetime. 2013.

[19] Z. Chang and S. Wang. Implications of primordial power spectra with statistical anisotropy on CMB temperature fluctuation and polarizations. 2013.

[20] B. Chen, R. Kantowski, and X. Dai. Embedded Lensing Time Delays, the Fermat Potential, and the Integrated Sachs-Wolfe Effect. *ArXiv e-prints*, 2013.

[21] L. Dai, D. Jeong, M. Kamionkowski, and J. Chluba. The pesky power asymmetry. Phys. Rev. D, 87(12):123005, 2013.

[22] G. D'Amico, R. Gobbetti, M. Kleban, and M. Schillo. Large-scale anomalies from primordial dissipation. *J. Cosmol. Astropart. Phys.*, 11:13, 2013.

[23] J. F. Donoghue, K. Dutta, and A. Ross. Nonisotropy in the CMB power spectrum in single field inflation. Phys. Rev. D, 80(2):023526, 2009.

[24] A. L. Erickcek, S. M. Carroll, and M. Kamionkowski. Superhorizon perturbations and the cosmic microwave background. Phys. Rev. D, 78(8):083012, 2008.

[25] A. L. Erickcek, C. M. Hirata, and M. Kamionkowski. A scale-dependent power asymmetry from isocurvature perturbations. Phys. Rev. D, 80(8):083507, 2009.

[26] A. L. Erickcek, M. Kamionkowski, and S. M. Carroll. A hemispherical power asymmetry from inflation. Phys. Rev. D, 78(12):123520, 2008.

[27] H. K. Eriksen, A. J. Banday, K. M. Górski, F. K. Hansen, and P. B. Lilje. Hemispherical Power Asymmetry in the Third-Year Wilkinson Microwave Anisotropy Probe Sky Maps. *Astrophys. J. Lett.*, 660:L81–L84, 2007.

[28] H. K. Eriksen, F. K. Hansen, A. J. Banday, K. M. Górski, and P. B. Lilje. Asymmetries in the Cosmic Microwave Background Anisotropy Field. ApJ, 605:14–20, April 2004.

[29] H. Firouzjahi, J.-O. Gong, and M. H. Namjoo. Scale-dependent hemispherical asymmetry from general initial state during inflation. *J. Cosmol. Astropart. Phys.*, 11:37, 2014.

[30] S. Flender and S. Hotchkiss. The small scale power asymmetry in the cosmic microwave background. *J. Cosmol. Astropart. Phys.*, 9:33, 2013.

[31] S. Flender, S. Hotchkiss, and S. Nadathur. The stacked ISW signal of rare superstructures in ΛCDM. *JCAP*, 2:13, 2013.

[32] D. Foreman-Mackey, D. W. Hogg, D. Lang, and J. Goodman. emcee: The MCMC Hammer. *Publ. Astron. Soc. Pac.*, 125:306–312, 2013.

[33] C. Gordon, W. Hu, D. Huterer, and T. Crawford. Spontaneous isotropy breaking: A mechanism for CMB multipole alignments. Phys. Rev. D, 72(10):103002, 2005.

[34] K. M. Górski, E. Hivon, A. J. Banday, B. D. Wandelt, F. K. Hansen, M. Reinecke, and M. Bartelmann. HEALPix: A Framework for High-Resolution Discretization and Fast Analysis of Data Distributed on the Sphere. ApJ, 622:759–771, April 2005.

[35] B. R. Granett, M. C. Neyrinck, and I. Szapudi. An Imprint of Superstructures on the Microwave Background due to the Integrated Sachs-Wolfe Effect. ApJ, 683:L99–L102, August 2008.

[36] B. R. Granett, M. C. Neyrinck, and I. Szapudi. Dark Energy Detected with Supervoids and Superclusters. 2008.

[37] A. Hajian and T. Souradeep. Measuring the Statistical Isotropy of the Cosmic Microwave Background Anisotropy. *Astrophys. J. Lett.*, 597:L5–L8, 2003.

[38] D. Hanson and A. Lewis. Estimators for CMB statistical anisotropy. Phys. Rev. D, 80(6):063004, 2009.

[39] C. Hernández-Monteagudo and R. E. Smith. On the signature of z
0.6 superclusters and voids in the Integrated Sachs-Wolfe effect. *MNRAS*, 435:1094–1107, 2013.

[40] G. Hinshaw, D. Larson, E. Komatsu, D. N. Spergel, et al. Nine-year Wilkinson Microwave Anisotropy Probe (WMAP) Observations: Cosmological Parameter Results. *ApJS*, 208:19, 2013.

[41] G. Hinshaw, J. L. Weiland, R. S. Hill, N. Odegard, D. Larson, et al. Five-Year Wilkinson Microwave Anisotropy Probe Observations: Data Processing, Sky Maps, and Basic Results. *ApJS*, 180:225–245, 2009.

[42] J. Hoftuft, H. K. Eriksen, A. J. Banday, K. M. Górski, F. K. Hansen, and P. B. Lilje. Increasing Evidence for Hemispherical Power Asymmetry in the Five-Year WMAP Data. ApJ, 699:985–989, 2009.

[43] S. Hotchkiss, S. Nadathur, S. Gottlöber, I. T. Iliev, A. Knebe, W. A. Watson, and G. Yepes. The Jubilee ISW Project - II. Observed and simulated imprints of voids and superclusters on the cosmic microwave background. MNRAS, 446:1321–1334, January 2015.

[44] D. Jeong, J. Chluba, L. Dai, M. Kamionkowski, and X. Wang. Effect of aberration on partial-sky measurements of the cosmic microwave background temperature power spectrum. Phys. Rev. D, 89(2):023003, 2014.

[45] M. Kamionkowski, A. Kosowsky, and A. Stebbins. Statistics of cosmic microwave background polarization. Phys. Rev. D, 55:7368–7388, June 1997.

[46] S. Kanno, M. Sasaki, and T. Tanaka. A viable explanation of the CMB dipolar statistical anisotropy. *Progress of Theoretical and Experimental Physics*, 2013(11):110001, 2013.

[47] R. E. Kass and A. E. Raftery. Bayes factors. *Journal of the American Statistical Association*, 90(430):773–795, 1995.

[48] S. C. Keller, B. P. Schmidt, et al. The SkyMapper Telescope and The Southern Sky Survey. *PASA*, 24:1–12, 2007.

[49] A. Kogut, D. J. Fixsen, D. T. Chuss, J. Dotson, E. Dwek, M. Halpern, G. F. Hinshaw, S. M. Meyer, S. H. Moseley, M. D. Seiffert, D. N. Spergel, and E. J. Wollack. The Primordial Inflation Explorer (PIXIE): a nulling polarimeter for cosmic microwave background observations. J. Cosmology Astropart. Phys., 7:025, July 2011.

[50] K. Kohri, C.-M. Lin, and T. Matsuda. Scale-dependent CMB asymmetry from primordial configuration. *J. Cosmol. Astropart. Phys.*, 8:26, 2014.

[51] A. Kosowsky. The Atacama Cosmology Telescope project: A progress report. *New Astronomy Reviews*, 50:969–976, December 2006.

[52] A. Kosowsky and T. Kahniashvili. Signature of Local Motion in the Microwave Sky. Phys. Rev. Lett., 106(19):191301, 2011.

[53] A. Kovács and B. R. Granett. Cold imprint of supervoids in the cosmic microwave background re-considered with Planck and Baryon Oscillation Spectroscopic Survey DR10. MNRAS, 452:1295–1302, September 2015.

[54] M. Levi, C. Bebek, T. Beers, R. Blum, R. Cahn, D. Eisenstein, B. Flaugher, K. Honscheid, R. Kron, O. Lahav, P. McDonald, N. Roe, D. Schlegel, and representing the DESI collaboration. The DESI Experiment, a whitepaper for Snowmass 2013. *ArXiv e-prints*, August 2013.

[55] A. R. Liddle. Information criteria for astrophysical model selection. MNRAS, 377:L74–L78, May 2007.

[56] A. R. Liddle and M. Cortês. Cosmic Microwave Background Anomalies in an Open Universe. Phys. Rev. Lett., 111(11):111302, 2013.

[57] Z.-G. Liu, Z.-K. Guo, and Y.-S. Piao. Obtaining the CMB anomalies with a bounce from the contracting phase to inflation. Phys. Rev. D, 88(6):063539, 2013.

[58] Z.-G. Liu, Z.-K. Guo, and Y.-S. Piao. CMB anomalies from an inflationary model in string theory. *European Physical Journal C*, 74:3006, 2014.

[59] LSST Science Collaboration, P. A. Abell, J. Allison, S. F. Anderson, J. R. Andrew, J. R. P. Angel, L. Armus, D. Arnett, S. J. Asztalos, T. S. Axelrod, and et al. LSST Science Book, Version 2.0. *ArXiv e-prints*, December 2009.

[60] D. H. Lyth. The CMB modulation from inflation. *J. Cosmol. Astropart. Phys.*, 8:7, 2013.

[61] J. C. Mather, E. S. Cheng, D. A. Cottingham, R. E. Eplee, Jr., D. J. Fixsen, T. Hewagama, R. B. Isaacman, K. A. Jensen, S. S. Meyer, P. D. Noerdlinger, S. M. Read, L. P. Rosen, R. A. Shafer, E. L. Wright, C. L. Bennett, N. W. Boggess, M. G. Hauser, T. Kelsall, S. H. Moseley, Jr., R. F. Silverberg, G. F. Smoot, R. Weiss, and D. T. Wilkinson. Measurement of the cosmic microwave background spectrum by the COBE FIRAS instrument. ApJ, 420:439–444, January 1994.

[62] A. Mazumdar and L. Wang. CMB dipole asymmetry from a fast roll phase. *J. Cosmol. Astropart. Phys.*, 10:49, 2013.

[63] J. McDonald. Hemispherical power asymmetry from scale-dependent modulated reheating. *J. Cosmol. Astropart. Phys.*, 11:41, 2013.

[64] J. McDonald. Isocurvature and curvaton perturbations with red power spectrum and large hemispherical asymmetry. *J. Cosmol. Astropart. Phys.*, 7:43, 2013.

[65] J. McDonald. Hemispherical power asymmetry from a space-dependent component of the adiabatic power spectrum. Phys. Rev. D, 89(12):127303, 2014.

[66] Adam Moss, Douglas Scott, James P. Zibin, and Richard Battye. Tilted physics: A cosmologically dipole-modulated sky. *Phys. Rev. D*, 84:023014, 2011.

[67] M. H. Namjoo, A. Akbar Abolhasani, S. Baghram, and H. Firouzjahi. CMB hemispherical asymmetry: long mode modulation and non-Gaussianity. *J. Cosmol. Astropart. Phys.*, 8:2, 2014.

[68] M. H. Namjoo, S. Baghram, and H. Firouzjahi. Hemispherical asymmetry and local non-Gaussianity: A consistency condition. Phys. Rev. D, 88(8):083527, 2013.

[69] P. Pápai, I. Szapudi, and B. R. Granett. Integrated Sachs-Wolfe Imprint of Superstructures on Linear Scales. ApJ, 732:27, 2011.

[70] Planck Collaboration, R. Adam, P. A. R. Ade, N. Aghanim, Y. Akrami, M. I. R. Alves, M. Arnaud, F. Arroja, J. Aumont, C. Baccigalupi, et al. Planck 2015 results. I. Overview of products and scientific results. *ArXiv e-prints*, February 2015.

[71] Planck Collaboration, P. A. R. Ade, N. Aghanim, Y. Akrami, P. K. Aluri, M. Arnaud, M. Ashdown, J. Aumont, C. Baccigalupi, A. J. Banday, et al. Planck 2015 results. XVI. Isotropy and statistics of the CMB. *ArXiv e-prints*, June 2015.

[72] Planck Collaboration, P. A. R. Ade, N. Aghanim, M. I. R. Alves, C. Armitage-Caplan, M. Arnaud, M. Ashdown, F. Atrio-Barandela, J. Aumont, H. Aussel, et al. Planck 2013 results. I. Overview of products and scientific results. A&A, 571:A1, November 2014.

[73] Planck Collaboration, P. A. R. Ade, N. Aghanim, C. Armitage-Caplan, M. Arnaud, M. Ashdown, F. Atrio-Barandela, J. Aumont, C. Baccigalupi, A. J. Banday, et al. Planck 2013 results. XII. Diffuse component separation. A&A, 571:A12, November 2014.

[74] Planck Collaboration, P. A. R. Ade, N. Aghanim, C. Armitage-Caplan, M. Arnaud, M. Ashdown, F. Atrio-Barandela, J. Aumont, C. Baccigalupi, A. J. Banday, et al. Planck 2013 results. XVI. Cosmological parameters. A&A, 571:A16, November 2014.

[75] Planck Collaboration, P. A. R. Ade, N. Aghanim, C. Armitage-Caplan, M. Arnaud, M. Ashdown, F. Atrio-Barandela, J. Aumont, C. Baccigalupi, A. J. Banday, et al. Planck 2013 results. XXIII. Isotropy and statistics of the CMB. A&A, 571:A23, November 2014.

[76] Planck Collaboration, P. A. R. Ade, N. Aghanim, M. Arnaud, M. Ashdown, J. Aumont, C. Baccigalupi, A. J. Banday, R. B. Barreiro, N. Bartolo, et al. Planck 2015 results. XXI. The integrated Sachs-Wolfe effect. *ArXiv e-prints*, February 2015.

[77] Planck Collaboration, N. Aghanim, C. Armitage-Caplan, M. Arnaud, M. Ashdown, F. Atrio-Barandela, J. Aumont, C. Baccigalupi, A. J. Banday, R. B. Barreiro, J. G. Bartlett, et al. Planck 2013 results. XXVII. Doppler boosting of the CMB: Eppur si muove. A&A, 571:A27, November 2014.

[78] Planck Collaboration, N. Aghanim, M. Arnaud, M. Ashdown, J. Aumont, C. Baccigalupi, A. J. Banday, R. B. Barreiro, J. G. Bartlett, N. Bartolo, and et al. Planck 2015 results. XI. CMB power spectra, likelihoods, and robustness of parameters. *ArXiv e-prints*, July 2015.

[79] S. Prunet, J.-P. Uzan, F. Bernardeau, and T. Brunier. Constraints on mode couplings and modulation of the CMB with WMAP data. Phys. Rev. D, 71(8):083508, 2005.

[80] M. Quartin and A. Notari. On the significance of power asymmetries in Planck CMB data at all scales. J. Cosmology Astropart. Phys., 1:008, January 2015.

[81] P. K. Rath and P. Jain. Testing the dipole modulation model in CMBR. *J. Cosmol. Astropart. Phys.*, 12:14, 2013.

[82] R. K. Sachs and A. M. Wolfe. Perturbations of a Cosmological Model and Angular Variations of the Microwave Background. ApJ, 147:73, January 1967.

[83] R. E. Smith, J. A. Peacock, A. Jenkins, S. D. M. White, C. S. Frenk, F. R. Pearce, P. A. Thomas, G. Efstathiou, and H. M. P. Couchman. Stable clustering, the halo model and non-linear cosmological power spectra. *MNRAS*, 341:1311–1332, 2003.

[84] The Dark Energy Survey Collaboration. The Dark Energy Survey. *ArXiv Astrophysics e-prints*, October 2005.

[85] L. Wang and A. Mazumdar. Small non-Gaussianity and dipole asymmetry in the cosmic microwave background. Phys. Rev. D, 88(2):023512, 2013.

[86] W. A. Watson et al. The Jubilee ISW project - I. Simulated ISW and weak lensing maps and initial power spectra results. *MNRAS*, 438:412–425, 2014.